Physics and Chemistry of the Earth 99 (2017) 3–21

Contents lists available at ScienceDirect

Physics and Chemistry of the Earth

journal homepage: www.elsevier.com/locate/pce

In situ interactions between Opalinus Clay and Low Alkali Concrete

Catherine Lerouge [a, *], Stéphane Gaboreau [a], Sylvain Grangeon [a], Francis Claret [a], Fabienne Warmont [b], Andreas Jenni [c], Veerle Cloet [d], Urs Mäder [c]

[a] BRGM, BP 6009, 45060 Orléans Cedex 2, France
[b] CNRS-CEMHTI UPR 3079, 1D Avenue de la Recherche Scientifique, 45071 Orléans Cedex 2, France
[c] RWI, Institute of Geological Sciences, University of Bern, Baltzerstrasse 3, CH-3012 Bern, Switzerland
[d] Nagra, Hardstrasse 73, 5430 Wettingen, Switzerland

ARTICLE INFO

Article history:
Received 30 August 2016
Received in revised form
9 January 2017
Accepted 13 January 2017
Available online 18 January 2017

Keywords:
Cement/clay interaction
Low pH cement
M-S-H
(Ca, Mg) smectite
Characterization
Mont Terri

ABSTRACT

A five-year-old interface between a Low Alkali Concrete (LAC) formulation (CEM III/B containing 66% slag and 10% nano-silica) and Opalinus Clay (OPA) from a field experiment at Mont Terri Underground Rock Laboratory in Switzerland (Jenni et al., 2014) has been studied to decipher the textural, mineralogical and chemical changes that occurred between the two reacting materials.

Reactivity between LAC concrete and OPA is found to be limited to a ~1 mm thick highly porous (ca. 75% porosity) white crust developed on the concrete side. Quantitative mineralogical mapping of the white crust using an electron microprobe and infrared spectroscopy on the cement matrix provides evidence of a Mg-rich phase accounting for approximatively 25 wt % of the matrix associated with 11 wt % of calcite, calcium silicate hydrate (C-S-H) and other cement phases. EDX analyses and electron diffraction combined with transmission electron microscopy of the Mg-rich phase provide evidence for a tri-octahedral 2:1 phyllosilicate with mean composition:

$(Ca_{0.5\pm0.2})$ $(Mg_{2.0\pm0.4}, Fe_{0.2\pm0.1}, Al_{0.5\pm03}, \square_{0.3\pm0.3})$ $(Al_{0.9\pm0.2}, Si_{3.1\pm0.2})$ O_{10} $(OH)_2$, where □ represents vacancies in the octahedral site.

Apart from this reactive contact, textural, mineralogical and chemical modifications at the contact with the LAC concrete are limited. OPA mineralogy remains largely unmodified. X-ray micro-fluorescence and EPMA mapping of major elements on the OPA side also provides evidence for a Mg-enriched 300 −400 μm thick layer. The cation exchange capacity (CEC) values measured in the OPA in contact with the LAC concrete range between 153 and 175 meq kg^{-1} of dry OPA, close to the reference value of 170 ± 10 meq kg^{-1} of dry OPA (Pearson et al., 2003). Changing cation occupancies at the interface with LAC concrete are mainly marked by increased Ca, Mg and K, and decreased Na. Leaching tests performed on OPA with deionized water and at different solid to water ratios strongly suggest that Cl and SO_4 have either conservative behaviour or are constrained by the solubility of a precipitated sulfate phase. The Cl and SO_4 concentrations measured at 2 cm from the interface are close to concentrations of undisturbed OPA pore waters (SO_4: 4.5 ± 1.5 mmol kg^{-1} of dry OPA; Cl: 7.5 ± 2.1 mmol $kg^{-1}$of dry OPA), and increase towards the interface with the concrete. The SO_4 to Cl ratio also increases towards the interface, suggesting that the increasing anion concentrations are not related to porosity variations but rather to a concentration gradient and sulfate phase precipitation near the interface.

1. Introduction

Geological disposal is now considered, in many countries, to be one of the best options for ensuring safe, long-term containment of radioactive waste. In many examples, a combination of waste overpacks (e.g. metal canisters, concrete), engineered barriers such as bentonite, and natural barriers such as clay rocks constitute the elements of the so-called “multiple-barrier system” between the waste matrix and the biosphere (Apted and Ahn, 2010; Chapman and Hooper, 2012). In repository facilities, the construction and exploitation phases and the presence of engineered barriers like silicate glasses (Debure et al., 2016; Gin et al., 2015; Poinssot et al., 2010), metal canisters (King and Shoesmith, 2010), and concrete

* Corresponding author.
E-mail address: c.lerouge@brgm.fr (C. Lerouge).

http://dx.doi.org/10.1016/j.pce.2017.01.005

(Alonso et al., 2010; Savage, 2014a, 2014b) will induce chemical gradients across the repository components that may alter the performance of the barriers over time (Bildstein and Claret, 2015).

Large volumes of cementitious materials will be used as backfill/barrier material or as structural support in a deep geological disposal facility for nuclear waste (ONDRAF/NIRAS, 2001; Nagra, 2002; Andra, 2005; SKB, 2006). By ensuring sorption capacity for radionuclides, gas storage capacity and a high pH environment to reduce corrosion, the cement backfill is an important safety barrier. In this context, the stability and performance of the cementitious material needs to be guaranteed. However, concrete will be in contact with the surrounding clayrock, bentonite and/or excavated clay materials, which could lead to chemical interactions that have an impact on sorption capacity, gas/water permeability and/or long-term stability of the cementitious material.

The contact between cementitious materials and clayey materials will induce diffusion of alkali-rich and high pH (12.5–13.5) pore cement solutions into the backfill (Berner, 1992). This alkaline plume will dissolve minerals such as montmorillonite or quartz at the favor of the formation of secondary phases like silicate hydrates, Ca aluminate silicate hydrates (C-(A)-SH), carbonates and possibly zeolites (Bartier et al., 2013; Bérubé et al., 1990; Cuevas, 2004; Gaboreau et al., 2011; Huertas et al., 2000; Ramirez et al., 2005; Savage, 2014a; Savage et al., 1992; Techer et al., 2012; Tinseau et al., 2006).

As it has been observed at interfaces between clay and cementitious materials, the extent of detectable perturbations in both materials is highly dependent on the nature of cementitious materials. Adapting the concrete recipe has therefore been a common approach to limit the interactions. Indeed regarding cement-based materials, recipes are numerous. Ordinary Portland cement-based (OPC) formulations are the most frequently considered. These cements, once hydrated, induce high alkaline concentrations and high pH (pH > 13.2). Although CEM I, which is made of finely ground Portland clinker, and CEM V, which is made of blended Portland, fly ash and blast furnace slag cement, are considered to be relevant cement materials (Chen et al., 2012) for nuclear waste repository condition, “low pH” cement recipes have been developed to limit the interactions (García Calvo et al., 2010; García Calvo et al., 2013; Lothenbach et al., 2012, 2014). By adding pozzolan and blastfurnace slag (Codina et al., 2008), low pH cements have (i) a low-heat development during hydration, which minimizes microcracking that can have negative consequences on the long-term durability, and (ii) low alkali contents, which limit the impact on clay in contact with this material compared to OPC.

Numerous experimental (Adler et al., 1999; Bauer and Berger, 1998; Dauzères, 2010; Devol-Brown et al., 2007; Eberl et al., 1993; Gaboreau et al., 2012; Ramirez et al., 2005; Read et al., 2001) and in situ studies (Bartier et al., 2013; De Windt et al., 2008; Gaboreau et al., 2011, 2012; Mäder et al., 2017; Techer et al., 2012) have investigated OPC and clay host rock interactions. Development of low pH concrete is more recent so the impact of low pH cement materials on surrounding clay host rocks has not yet been investigated as extensively (Dauzères et al., 2016; Jenni et al., 2014; Savage and Benbow, 2007). Experiments have been performed to mimic in situ interaction of low pH cement with claystone, providing evidence of strong degradation in cement material inducing increased porosity, and of specific mineralogical changes including a new hydrated Mg-Si phase (Dauzères et al., 2014).

Since April 2007, a long-term in situ Cement-Clay interaction (CI) experiment has been running at the Mont Terri Rock Laboratory (St. Ursanne, Switzerland). Its goal is to understand processes occurring at concrete/clay interfaces. The textural properties, mineralogy and chemistry are investigated on interfaces between OPA, bentonite and different concrete materials Portland cement, ESDRED shotcrete cement and a Low Alkali low-pH Cement (named LAC in the following) over time under realistic conditions (Jenni et al., 2014; Mäder et al., 2017). Previous in situ characterization of the LAC concrete provided evidence of a Mg-rich white crust and the formation of a Mg-bearing cement phase (also called M-S-H) at the interface with OPA due to a Mg gradient from the clay formation to the concrete (Dauzères et al., 2016; Jenni et al., 2014). The objective of this work is to present a multi-scale approach to obtain physical, mineralogical and chemical data of OPA and the LAC concrete in contact with each other after five years of interaction, with a specific mineralogical and chemical focus on the Mg-bearing cement phase.

2. Materials, sampling and analytical strategy

The CI experiment is located in the HE-D niche adjacent to Gallery-98 that was excavated in 1998 (Jenni et al., 2014; Mäder et al., 2017). This niche is located in the shaly facies of Opalinus Clay with a clay content of ~60 wt% (Jenni et al., 2014; Lerouge et al., 2015; Pearson et al., 2003). The CI experiment consists of two vertical boreholes (368 mm diameter and up to 9 m long) in OPA, filled with sections of three different concretes (a CEM I Portland cement: OPC, and two low-pH cements: LAC and ESDRED) and a section of compacted bentonite (Jenni et al., 2014; Mäder et al., 2017). The LAC concretes were emplaced below the Excavation Disturbed Zone (EDZ) of the main tunnel, in the undisturbed saturated zone. Precautions were taken to prevent drying out of the Opalinus Clay during drilling of the boreholes.

This study specifically concerns the interface between the low-alkali LAC concrete and OPA after 5 years. The LAC cement was a mix of 90% of CEM III/B 42.5 L (66% of slag+34% of clinker) with 10% of nanosilica corresponding to a ternary mix of 10% of nanosilica, 59% of slag, and 31% of clinker. The LAC concrete was prepared at a water to cement ratio of 1 with addition of polycarboxylate-based superplasticizer (Lothenbach et al., 2012) and by adding sand and gravel as aggregates. Material suppliers were Jura Cement Switzerland (CEMIII/B 42.5 L “JURANIT”), Degussa Switzerland (nanosilica “Aerosil 200”, superplasticizer “Glenium C321”) and TFB Switzerland (sand and gravel, according to SN EN 12620, rounded river sediment). The pore water chemistry of the LAC hydrated cement paste is given in Lothenbach et al. (2012); the pH of the pore solution is 12.3 ± 1.0. Previous characterizations of the interface between the LAC concrete and OPA after 2.2 years and 5 years are reported by Jenni et al. (2014) and Dauzères et al. (2016).

A piece of the core sample containing the interface between the LAC concrete and OPA after 5 years was embedded in a resin to prevent OPA dehydration and to maintain interface cohesion (Fig. 1a). The contact between claystone and concrete is cohesive and continuous. The OPA side is highly fissured, and contains a centimetre-scale bivalve fossil (Fig. 1b). A ~1 mm thin layer of concrete in contact with OPA has a whitish colour, an obvious product of interaction.

A centimetre-thick section of the sample was cut to make an impregnated polished section for autoradiography and electron microprobe mapping, in order to determine the spatial distribution of porosity and to quantify the minerals in the white crust. Another centimetre-thick section through the plane of the LAC concrete/OPA interface was used for chemical analyses and further mineral investigations on the white crust. This section was roughly polished and then glued onto a glass section. The sample was cut with a saw without water to obtain a 1 mm thick section that was polished for observation. The rest of the section was used to obtain powder samples of the clay rock and concrete. The concrete and claystone were separated at the interface and regularly sampled using a micro-drill and starting the sampling sequence from the interface.

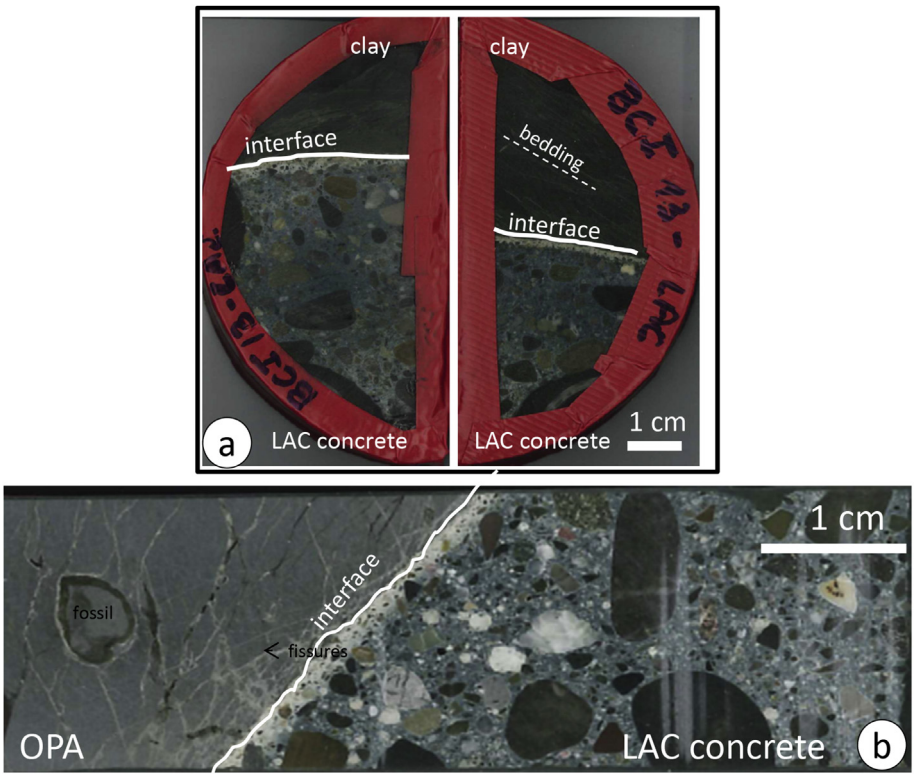

Fig. 1. (a) Core sample crosscutting the interface between the LAC concrete and OPA embedded in a resin; (b) sample section used for the detailed sampling.

Samples were taken at small intervals near the concrete/clay interface and at large intervals further from the interface (0–1 mm, 1–5 mm, 5–10 mm, 10–20 mm). The minimum interval thickness was set at about 1–2 mm in order to obtain enough powder for all the analyses. Each sample was weighed, crushed and sieved with a cut-off diameter of 80 μm, with the exception of an aliquot of the white crust of the LAC concrete, which was separated and sieved without crushing, with the aim of removing the aggregates (sieved LAC 0–1 mm).

Preparing the samples in this way means that we could use a set of analytical techniques that were appropriate for the scale and for characterization of the textural, mineralogical and chemical evolution of both materials in a complementary way. Textural perturbations were identified by microscopic observations and estimated by porosity measurements using autoradiography. Major chemical perturbations were identified by element mapping of the interface using X-ray micro-fluorescence and electron microprobe, completed by aqueous leaching tests and cationic exchange measurements in OPA. Cation and anion concentrations of pore waters in perturbed claystone were deduced from these data and compared with those of unperturbed claystone. Powder X-ray diffraction and infrared spectrometry were performed on bulk concrete and OPA both at the interface and far from the interface, to identify mineralogical perturbation of both materials.

Further mineralogical investigations were carried out on the sieved aliquot of the white crust (sieved 0–1 mm LAC) to pursue mineralogical and chemical investigations on the M-S-H phase already identified (Dauzères et al., 2016; Jenni et al., 2014). The chemical composition of the M-S-H phase was determined using a combination of electron microprobe and transmission electron microscope coupled with EDX analyses, whereas the crystalline structure of the M-S-H phase was investigated using powder X-ray diffraction, Fourier-transform infrared spectroscopy, Raman spectrometry, ^{29}Si Nuclear Magnetic resonance, and electron diffraction.

3. Analytical techniques

3.1. Autoradiography

The in situ porosity was calculated from autoradiography using the method developed by Prêt (2003) for clay materials. The impregnation conditions adapted for the cement materials were chosen according to the work of Galle (2001), which showed the impact of drying on cement materials. The sample was oven-dried for 20 days at 75 °C under vacuum. The sample was then impregnated for 40 days with ^{14}C Methylmethacrylate (MMA) with tracer activity of 4.6 μCi/mL. The objective was for the resin to achieve a total porosity saturation in order to obtain quantitative porosity measurements by autoradiography. The polymerization is induced by ^{60}Co irradiation with a total dose of 120 kGy (Prêt, 2003). The textural state of the impregnated sample is expected to be close to the textural state encountered for sample in equilibrium with water in response to the resin properties (viscosity and dipole moment) that are close to those of water (Prêt et al., 2010). Two polished sections were prepared with a low-speed diamond saw by cutting the sample in half. They were polished using diamond powders with grain sizes down to 0.05 μm. The thick sections were then exposed on Kodak Biomax MR film for 7 days. Exposure times were optimized according to the varying claystone and cement material porosities to acquire the best porosity contrast (Prêt, 2003). The autoradiographs were then digitized in 8 bit images with a resolution of 2400 dpi (10.4 × 10.4 μm^2 pixel size). The local blackening of the film (expressed by a local optical density) is proportional to the local concentration of radioactive resin. A set of calibration sources of known activity were simultaneously exposed on the

autoradiograph films to obtain the relationship between the local activities and optical densities. The experimental data were fitted using the calibration function proposed by Hellmuth et al. (1993). A local mean porosity was then calculated for each pixel of the digitized autoradiograph from the calibration function and tracer activity using the relationships provided by Sammartino et al. (2002) and the in house autoradio software (Prêt, 2003). Local pixel porosities include the connected micro-, meso-, and macro-porosity. For each autoradiograph, a combination of analysis methods was used to reveal the porosity distribution. Porosity frequency histograms were computed on different sub-areas of the autoradiograph by counting the number of pixels having similar porosity values. To localize the spatial heterogeneities, porosity maps were then computed by displaying the local porosity of each pixel using a linear grey level scale ranging between two porosity values identified on the histogram. Porosity profiles were computed to reveal changes in porosity as a function of two distal points. Profiles were calculated for one pixel along a straight line (1 pixel width) or dilating the straight line by a given number of pixels in width to reach average porosities with improved statistical error.

3.2. X-ray micro-fluorescence (μXRF) mapping

μXRF was used to characterize spatial heterogeneities by mapping some major chemical elements (Ca, Mg, K, Al, Fe, S and Si) on polished sections sampled every centimetre through the interface from the concrete material to the undisturbed claystone. Although Na is an important element for understanding the diffusion process, the Na map is not presented because this light element was barely detectable with this spectrometer. μXRF measurements were carried out under vacuum on a HORIBA XGT-7000 microscope equipped with an X-ray guide tube producing a focused and high-intensity beam with a 10 μm or 100 μm spot size, respectively. The X-ray beam was generated with a Rhodium X-ray tube at an acceleration voltage of 30 kV with a filament heating current of 1 mA. The samples were fixed on a xyz motorized table, z being adjusted at the focal plane with an optical camera. X-ray emission from the irradiated sample was detected with an Energy-Dispersive X-ray (EDX) spectrometer equipped with a liquid-nitrogen-cooled high purity Si detector. Detector resolution was 145 eV at the Mn Kα emission line. XRF analyses presented a detection limit (near 100 mg kg^{-1} depending on the element) lower than that obtained with SEM-EDX. Maps of the whole samples (512 × 248 pixels) were obtained using the 100 μm monocapillary, scanning the samples in x and y directions. Twenty 1000 s frames were collected and added to obtain the element maps. Each map corresponds to raw counts.

3.3. Leaching and cation exchange capacity on OPA

Leaching and cation exchange capacity (CEC) measurements were performed on about 100–200 mg of dry powder in a glove box under nitrogen atmosphere. Rock/water ratios were 10, 20 and 100 g/L for leaching and 50 g/L for CEC. Detailed procedures are given in Jenni et al. (2014). The leaching tests were applied at three solid/liquid ratios to verify if anions are conservative or not. When the anion concentration is correlated with the solid/liquid ratio, the behaviour of the anion is conservative or semi-conservative which indicates that the anion concentration measured in the leachate may be considered as representative of the anion concentration in the pore water of the clayrock, taking account the anion-accessible porosity factor according to Gaucher et al. (2006), and not related to the dissolution of a mineral phase.

3.4. X-ray diffraction (XRD)

The XRD patterns were recorded with a SIEMENS D5000 powder diffractometer using Co Kα radiation (λ = 0.1789 nm) and operated at 40 kV and 100 mA. Intensities were recorded at a 0.02°(2θ)/10 s scanning rate from 4 to 84°.

3.5. Infrared spectrometry (IR)

Infrared spectra were obtained on a BRUKER Equinox IFS55 spectrometer by transmission through a pellet made of a mixture of 150 mg KBr with about 0.5 mg of sample. For each spectrum, 32 scans were performed from 4000 to 350 cm^{-1}. The spectral resolution for this study was always 4 cm^{-1}. Spectra were normalized to pure calcite (Omya) for calcite quantification, and to synthetic M-S-H with Ca/Si ratio of 0.6 (Roosz et al., 2015) for approximate M-S-H quantification.

3.6. Raman spectrometry

Raman measurements were performed in situ on thin polished sections with a Renishaw InVIA Reflex microspectrometer coupled to a DM Leica microscope equipped with 4 lenses with ×5, ×20,×50 and ×100 magnification. The excitation laser was an argon laser (λ_0 = 514.5 nm). Each spectrum was acquired with two accumulations and an acquisition time of 10 s, over a 200-1200 cm^{-1} spectral range. Calibration was done using the silicon 520.4 cm^{-1} line. Instrument control and Raman measurements were performed with Renishaw WIRE^{TM} software. Raman spectra acquired on the M-S-H phase were processed using the Fityk software (Wojdyr, 2010).

3.7. Nuclear magnetic resonance (NMR)

NMR was used to evaluate the structure of the Mg-bearing cement phase in the white crust separately. ^{29}Si MAS NMR spectra were acquired at 59 MHz on a Bruker AVANCE 7.4 T (300 322 MHz) spectrometer equipped with a 4 mm double bearing MAS probe-head spinning at 12 kHz. About 16,000 scans were accumulated after a 45° pulse, using 1 s recycling delay. This delay was optimized to ensure complete magnetization relaxation. ^{29}Si chemical shifts were reported relative to TMS resonance. The spectra were deconvoluted in individual Gaussian-Lorentzian bands, using the Dmfit program (Massiot et al., 2002).

3.8. Mineralogical characterization of concrete by imaging technique

Mineralogical maps can be built based on the combination of a set of chemical element maps according to the method developed by Prêt et al. (2010). Maps were acquired with a field of view of 1 × 1 mm^2. This is not representative for the complete mineralogy of the concrete since it is clearly smaller than the aggregate size. X-ray intensity maps of Si, Al, Fe, K, Na, Ca, Mg, Ti, Mn, and S were acquired using a Cameca SX Five electron microprobe (EPMA) with an accelerating voltage of 15 kV and a current beam of 30 nA. Using the electron microprobe allowed a high counting rate and a short dwell time (≈4 s) for quantitative point analysis. This dwell time is too time-consuming for the mapping mode, so a shorter counting time of 100 ms per pixel was used. To reduce the total acquisition time (2 days), the background was not measured or subtracted from X-ray emission peaks as its contribution at short dwell times and for high concentrations was low (Goldstein, 1992) and its recording would have doubled the acquisition time. We then applied a PHIRHOZ matrix correction (Merlet, 1994) to provide a

weight percentage for each element per pixel. The elemental maps were recorded by stage rastering using a stationary beam, with spatial resolution of 2 μm per pixel and containing 512 by 512 pixels. X-ray maps were then processed using the μMAPphase software (Prêt et al., 2010). The aim of this method is to identify the mineral phases present in the analysed area, from step by step projections of the scanned elemental composition points into ternary plots displaying the chemical compositions of all mineral phases. Each pixel of the initial quantitative X-ray maps is firstly converted into element weight percent (at wt %) followed by the conversion into element molar percent (at mol %). All pixels of the mapped area are plotted in ternary diagrams, where each axis of the plot represents the concentration of an element or a combination of elements. This method is not affected by porosity variations as normalized axis weights are used when generating ternary scatter plots. Several clusters of pixels can be identified in the chemical ternary plots. These clusters represent the chemical compositional fields of one mineral and their stoichiometry can be compared directly to the different mineral end-members by adding their theoretical compositions to the projection. In the case of phase mixtures occurring within the measurement volume, or solid solutions, clusters are stretched over a volume defined by several end-members. Pixels with similar chemical compositions (i.e. a cluster) are selected with a polygon tool and back-projected onto a mineral map using the same colour as the selected polygon.

3.9. Electron microprobe spot analyses

Chemical spot analyses of M-S-H phase were performed using the EPMA with an accelerating voltage of 15 kV, a beam current of 12 nA, a 1–2 μm beam width and a counting time of 10 s. Ca, K, Na, Mg, Si, Al, S and Fe were analysed. Ca-Kα and K-Kα were monitored on a LPET crystal, Na-Kα and Mg-Kα on a LTAP crystal, Si-Kα and Al-Kα on a TAP crystal, S-Kα on a PET crystal, Fe-Kα on a LLiF crystal. Standards used included both well-characterized natural minerals and synthetic oxides. Matrix corrections were made with a ZAF software program.

3.10. Scanning electron microscope (SEM)

Observations, analyses and element mapping were performed using a TESCAN MIRA 3 XMU FE scanning electron microscope (SEM) (Brno - Czech Republic) coupled with an EDS EDAX TEAM system (EDAX – USA) and a APOLLO XPP silicon drift detector at 25 kV. Prior to analysis, a thin carbon layer was sputter-coated on the samples (Edwards Auto 306, Genevilliers, France).

3.11. Transmission electron microscope (TEM)

TEM and EDX analyses were performed on finely divided cement materials of the white crust to examine the texture of the M-S-H phase and to estimate its chemical composition. Observations were carried out with a Philips CM20 microscope coupled with an EDAX EDX operated at 200 kV. The cement phase of the white crust was separated and slightly crushed between two glass plates to eliminate residual carbonate and quartz aggregates. Observations were made on two types of preparation deposited on carbon coated TEM copper grids: 1) a few micrograms of material dispersed in ultra-pure ethanol using an ultrasonic bath, and 2) several microtome thin sections of material embedded in LR white® resin. The data correspond to raw counts.

4. Autoradiography and quantitative porosity at the interface

A polished section prepared for autoradiography shows that the contact between the LAC concrete and OPA is composed of a ~1 mm thin white layer on the concrete side. Under the microscope at low magnification, the polished section does not give evidence of fracturing in the LAC concrete, whereas a dense fracture network affects OPA at the first centimetres near the interface. Three sets of fracture orientations can be distinguished. A main set of fractures corresponds to the rupture of the rock along the bedding planes (dashed line); this set is dense near the interface. The two other sets of fractures correspond to two planes of rock rupture (called P and P′) that are perpendicular to each other and oblique to bedding (Fig. 2). The P planes are visible near the interface, whereas the P' plans are more visible far from the interface. Under SEM and at high magnification, the cement paste shows randomly oriented microcracks developed in the white crust. This micro-fracturing could be due to dehydration of the cement material during preparation and resin embedding, or during vacuum pumping in the SEM chamber. Fractures in the first 5 mm of OPA near the interface are generally not sealed by mineral neoformation.

The porosity of both materials at the LAC concrete/OPA interface was investigated by autoradiography. Several porosity measurements in concrete, cement binder and OPA were performed on the autoradiograph of the interface (Fig. 2). Porosity was estimated by calculating the frequency histogram of the porosity distribution for each individual zone.

The mean porosity of concrete deduced from porosity measurements of large concrete surfaces including aggregates is 24% (Table 1: areas 8 to 11). This porosity value is high according to the reference value for such materials (Galle, 2001). The porosity measurements of the hydraulic binder indicate an increase of the porosity toward the interface, from ≈50% at several centimetres from the interface (Table 1: areas 14 and 15) to ≈75% in the first millimetre of concrete in contact with OPA (Table 1: areas 12 and 13), corresponding to the white crust (Fig. 2).

The mean porosity of Opalinus Clay deduced from porosity measurements of large OPA surfaces close to the interface is 24% (Table 1: area 1 to 3). The porosity measured far from the interface (OPA 1.5 cm) is 17–18% (Table 1: areas 4 and 5), a value that is consistent with the reference range for water content porosity for silty-shaly facies (16–20% in annex 10, Pearson et al., 2003). At the concrete interface, the porosity map gives evidence of a light-coloured layer that corresponds to increased claystone porosity of up to 44–48% (Table 1: areas 6 and 7), even though visible macroscopic cracks were absent for the measured area. This porosity value could be due to an increase of micro-fracture density as displayed on the porosity map developed in the clay matrix during sample preparation. This porosity increase impacts the mean porosity obtained on large OPA surfaces.

5. Chemical perturbation of the LAC concrete/OPA clay interface

5.1. Elemental mapping of polished sections using micro-XRF and electron microprobe

Mapping of major elements using micro-XRF and line profiles over 2.5 cm in both the OPA and LAC show that the major chemical changes are in the white crust corresponding to the first millimetre of concrete in contact with OPA (Fig. 3). By comparison with unperturbed LAC concrete, the white crust is slightly depleted in Ca and enriched in Al, Mg and S. It is noteworthy that the Mg enrichment in the white crust is the major chemical change, with the Mg content also significantly higher than the Mg content in OPA. The Mg profile through the white crust indicates that the Mg content increases progressively toward the interface. The increases in S and Al contents are more difficult to observe in the profiles.

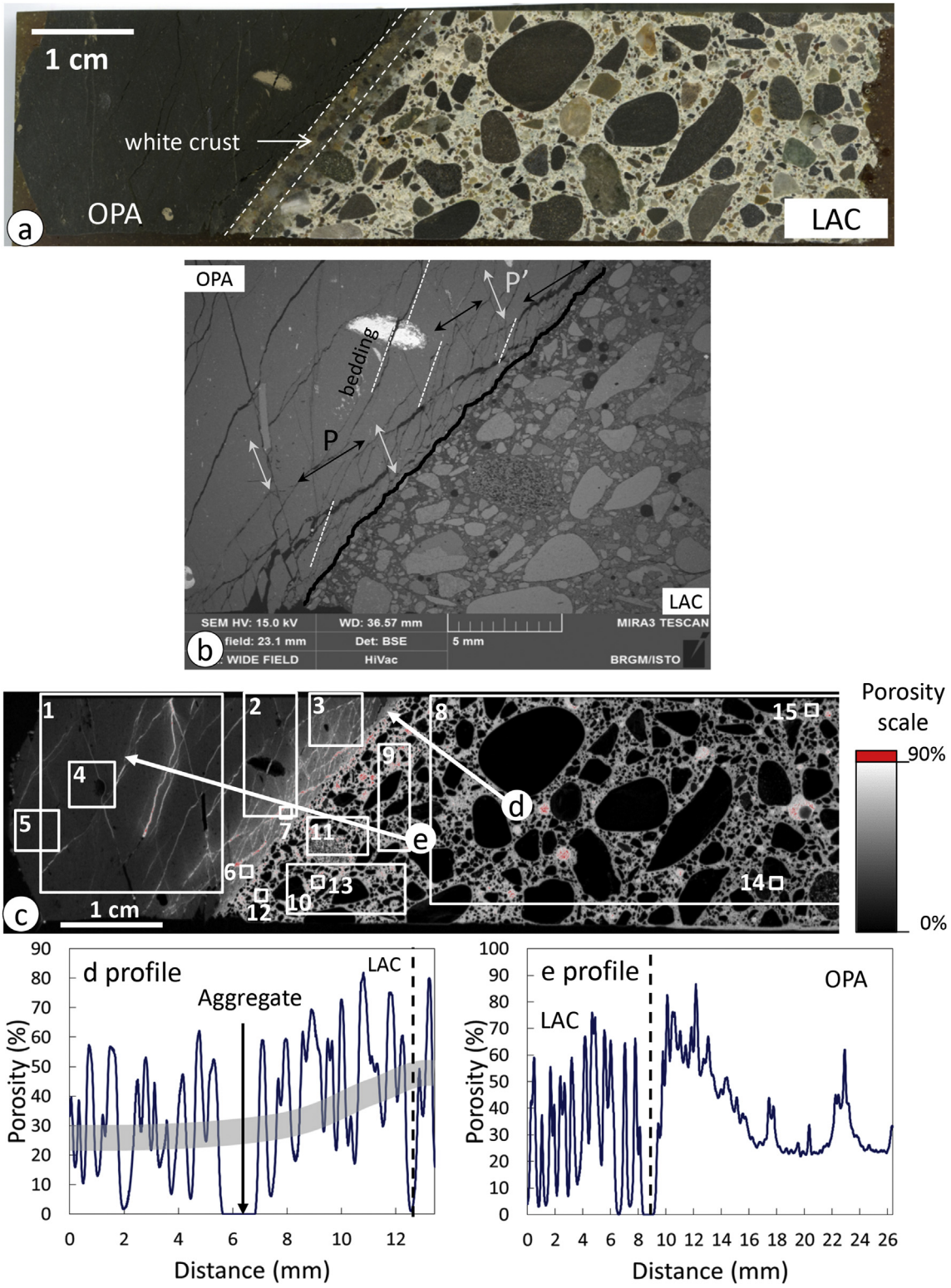

Fig. 2. (a) Autoradiograph sample; (b) BSE image of the interface showing the major orientations of fissuration P and P′ and the bedding (dashed lines) in OPA; (c) Porosity map calculated from the autoradiography results. The squares on autoradiography indicate the position of the different areas for which porosity was quantified and given in Table 1. The two arrows indicate the position and the direction sof the two profiles (d) and (e) on which porosity was quantified; (d) Porosity profile through LAC concrete toward the interface with OPA; (e) Porosity profile through the OPA/LAC interface. In the both porosity profiles, distance is given from the white point to the arrow, and the dotted lines represent the interface between LAC and OPA.

Outside the white crust, LAC concrete does not provide evidence of chemical change. On the OPA side, chemical changes at the interface are small, marked by possible slight increases of S and Mg contents. Complementary elemental mappings using SEM at high

Table 1
Measurements of the porosity of the different areas in both OPA and LAC concrete, using autoradiography. The positions of the areas are indicated in Fig. 2c.

LAC concrete			OPA		
Area	Position	Porosity (%)	Area	Position	Porosity (%)
8, 9, 10, 11	large areas concrete	24	1, 2, 3	large areas clay-rock	24
12	Hydraulic binder at the interface	75	4	Clay rock distant from interface	17
13		74	5		17
14	Hydraulic binder distant from the interface	54	6	Clay rock at the interface	39
15		50	7		44

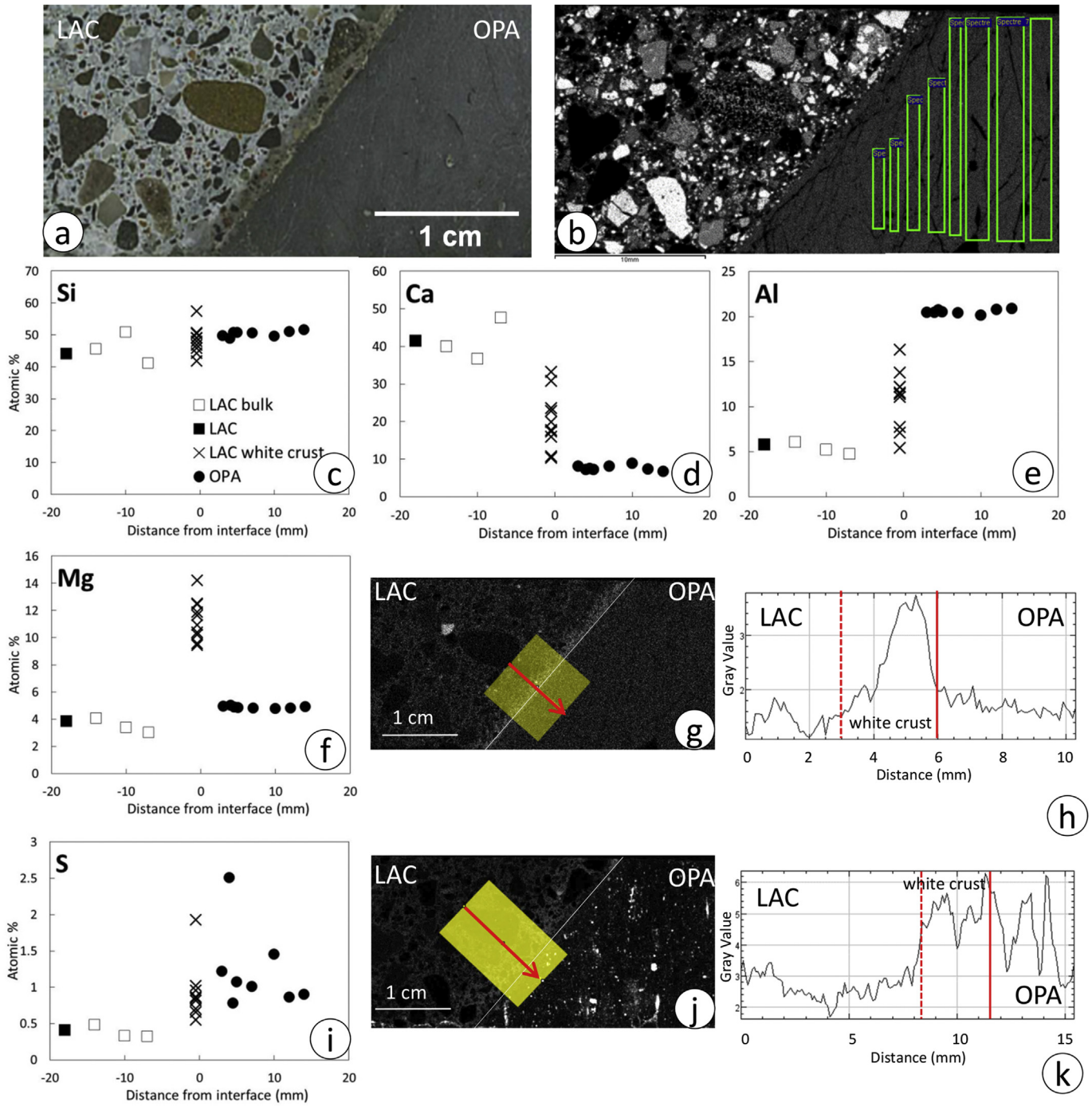

Fig. 3. (a) Autoradiograph sample used for micro XRF; (b) Position of zones analysed successively in OPA; (c) Profile of Si through the OPA/LAC interface; (d) Ca profile; (e) Al profile; (f) Mg profile; (g) Mg XRF map with location of a line profile through the interface; (h) Mg line profile; (i) S profile; (j) S XRF map with location of a line profile through the interface; (k) S line profile.

magnification confirm previous results in LAC concrete, but also provide evidence of low Al depletion on the OPA side near the interface and a ~300-500 μm-thick Mg-rich layer at ~500 μm far from the interface (Fig. 4).

5.2. Aqueous leaching of Opalinus Clay

The Cl, Br and SO_4 concentrations in leachate reported as a function of the solid/liquid ratios were proportional, strongly suggesting that these anions have conservative behaviour (Appendix A). On this assumption, anion concentrations were calculated in mmoles per kg of dry OPA and are reported as a function of the distance to the interface in Fig. 5. Anion concentrations were not recalculated in mmoles per litre of pore water due to the lack of water content measurements and due to the uncertainty in the porosity measurements. Between 0 and 2 cm from the interface, SO_4, Cl and Br concentrations decreased from 24 to 6 mmol kg^{-1} of dry OPA, from 13 to 10 mmol kg^{-1} of dry OPA and from 0.2 to 0.05 mmol kg^{-1} of dry OPA, respectively. These data provide evidence that 1) at 2 cm from the interface, the measured values are near the anion concentrations of well-preserved OPA pore waters (SO_4: 7.6 ± 3.0 mmol kg^{-1} of dry OPA; Cl: 10.0 ± 3.0 mmol kg^{-1} of dry OPA), and 2) the concentrations of all anions increase towards the interface with the concrete. However, the increases of Cl and SO_4 concentrations are not proportional. The higher increase of SO_4 indicates that SO_4 increase is not only due to porosity variations but probably also due to some dissolution of a sulfate phase.

5.3. Cation exchange capacity measurements on OPA

The cation exchange capacity (CEC) values measured for OPA in contact with the LAC concrete range between 153 and 175 meq/kg of dry OPA, whatever the distance to the interface, and are not significantly different from the reference value of 170 ± 10 meq/kg of dry OPA given in Pearson et al. (2003) obtained with the same method (Appendix B). For the samples between 5 and 20 mm, the

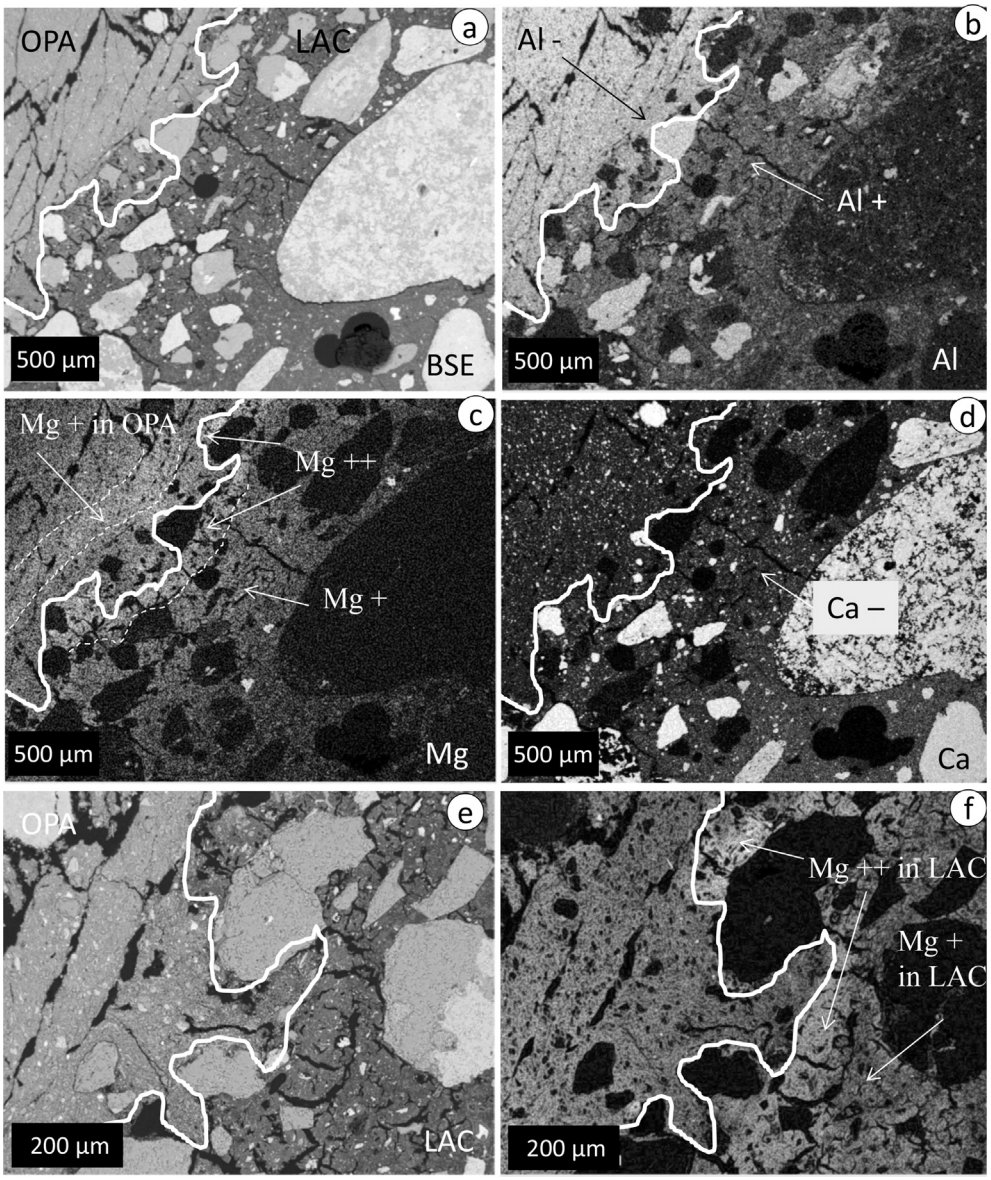

Fig. 4. Elemental mapping (Mg, Al, Ca, Si) of the OPA/LAC interface using SEM – (a) BSE image of a ~1.5 × 2.5 mm through the LAC/OPA interface; (b) Al map; (c) Mg map; (d) Ca map; (e) BSE image of a detail zone of interface; (f) Mg map.

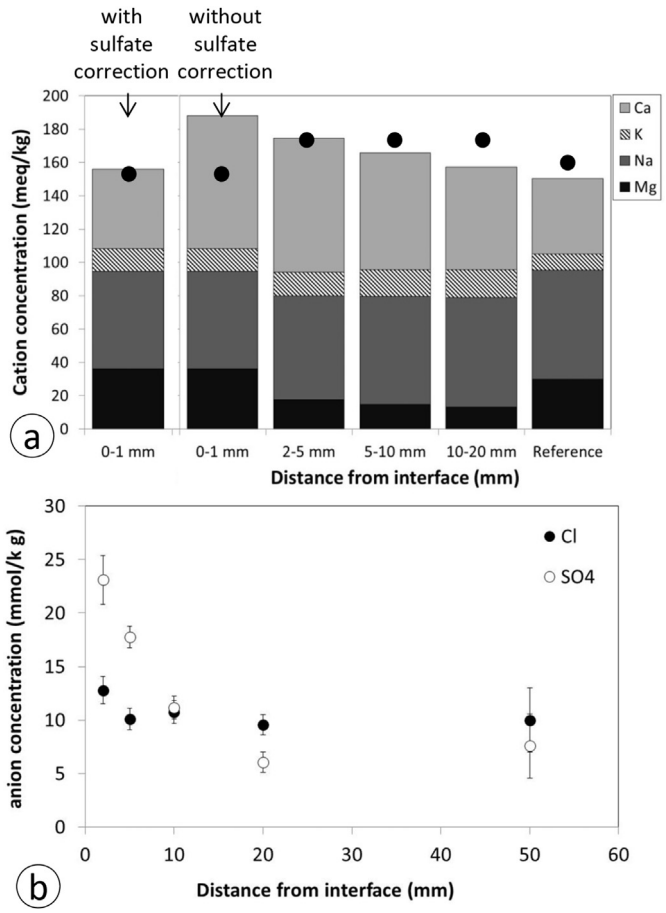

Fig. 5. CEC and aqueous leaching in OPA - (a) Concentrations of major cations sorbed on clay minerals measured by cobalt hexamine method as a function of distance toward the interface, and compared to OPA reference; CEC measurements by colorimetry (black circles) are superposed on the graph; (b) Profiles of sulphates and chlorides concentration of aqueous leachate in function of distance to interface. Values at 5 cm correspond to unperturbed OPA reference.

CEC value is almost equal to the sum of cations, suggesting that the cation concentrations can be considered as representative of the exchanger. Near the interface (0–5 mm), the sum of cations is higher than the CEC value. This slight inconsistency between the CEC and the sum of cations could be due to a partial dissolution of a mineral phase. The combined slight SO_4 increase in aqueous leachate and the abnormal increase of Ca concentration in the clay exchanger at interface suggest gypsum [$CaSO_4$] dissolution. Based on this assumption, a correction of Ca associated with the SO_4 increase for the same solid/liquid ratio was applied to Ca concentration in CEC leachate. With this correction, the CEC is in agreement with the sum of cations.

The cation exchanger towards the interface is chemically modified relative to OPA reference values. Chemical change is characterized by decreased Mg occupancy between 0.2 and 2 cm distance coupled with changes in K (increase towards the interface) and Ca (increase from 10-20 mm to 2–5 mm and then decrease towards the interface) (Fig. 5).

6. Mineralogical characterization at the LAC concrete/OPA clay interface

6.1. X-ray diffraction

The XRD patterns of the OPA in contact with the LAC concrete, near (OPA 0–1 mm) and far (OPA 10–20 mm) from the interface are very similar. The amounts of minerals estimated by treatment of XRD data in the both OPA samples near (OPA 0–1 mm) and far (OPA 10–20 mm) from the interface are almost identical taking into account uncertainties on the values, and remain in the range of values estimated in OPA reference, suggesting that there is no significant mineralogical change in the claystone during alkaline perturbation (Fig. 6a; Table 2). A detailed pattern between 5 and 22° 2θ CoKα provides evidence of clay minerals other than illite and illite-smectite mixed layers: kaolinite, muscovite, and chlorite.

Concrete samples in contact with OPA (LAC 0–1 mm) and far from OPA (LAC 10–20 mm) display almost identical XRD patterns and are mainly composed of calcite and quartz with minor albite, corresponding essentially to their aggregate content (Fig. 6b). The XRD pattern of the white crust (LAC 0–1 mm) reveals presence of quartz, calcite, albite, clay minerals such as chlorite and illite-mica, and three supplementary discrete maxima around 23°2θ CoKα, 41°2θ CoKα and 69°2θ CoKα (Fig. 6b). Their position and their relative intensities are consistent with those of synthetized M-S-H with Mg/Si ratio of 0.6 described by Roosz et al. (2015). These data, however, show that the Mg-bearing cement phase of the white crust poorly diffracts due to its nano-crystallinity, and is consequently difficult to detect in a bulk XRD pattern of concrete.

6.2. Microscopic observations

SEM observations were made to detect minerals which were not identified by XRD, and to detect any mineral dissolution or neoformation at a microscopic scale (Fig. 7). The white crust in the concrete at the OPA interface consists of quartz and carbonate aggregates, with residual clinkers in amorphous matrix of M-S-H phase, C-A-S-H with minor calcite. None of the mineral phases present naturally in OPA show any dissolution feature, except some grains of ankerite [$Ca(Fe, Mg)(CO_3)_2$] which are surrounded by a μm-sized corona of iron hydroxides. No trace of iron-oxi-hydroxides was observed in association with framboidal pyrite which is generally considered as most reactive to oxidation.

6.3. Infrared spectroscopy

Infrared (IR) spectra were normalized to the IR spectrum of a pure calcite (Omya), allowing direct comparison of all spectra and estimation of the calcite content. The IR spectra of OPA 0–1 mm and OPA 10–20 mm are almost identical for the positions and the intensities of the peaks and bands that correspond to the main claystone mineralogy: quartz, calcite and clay minerals (kaolinite, chlorite, illite) (Fig. 8 a, b, c). It is noteworthy that the clay content is slightly higher in OPA 10–20 mm than in OPA 0–2 mm, and the calcite content is about 10 wt % (wt %) in the both samples.

The IR spectra of bulk concrete (LAC 0–1 mm and LAC 10–20 mm) allowed evaluating the presence of cement phases as a function of the distance from the contact with OPA (Fig. 8 f). The bands at~1082, 1170, 798, 779, 516 and 460-470 cm^{-1} correspond to quartz. The bands at 1429, 877 and 712 cm^{-1} correspond to calcite. A small shoulder of the major peak at ~1400 cm^{-1} could correspond to dolomite. Quartz and calcite peaks are high in the two samples of bulk concrete; they essentially correspond to silicate and limestone aggregates. ~75 wt % and ~28 wt % of calcite were estimated, respectively, in LAC 0–1 mm and LAC 10–20 mm. No portlandite or other cement phase was clearly identified by infrared spectroscopy.

To obtain a better signal on the cement matrix additional IR spectra were acquired on the sieved fraction of the white crust (sieved LAC 0–1 mm). Quartz and calcite signals were significantly attenuated, indicating that the slight grinding combined with sieving is efficient. About 11 wt % of calcite remained in the sieved

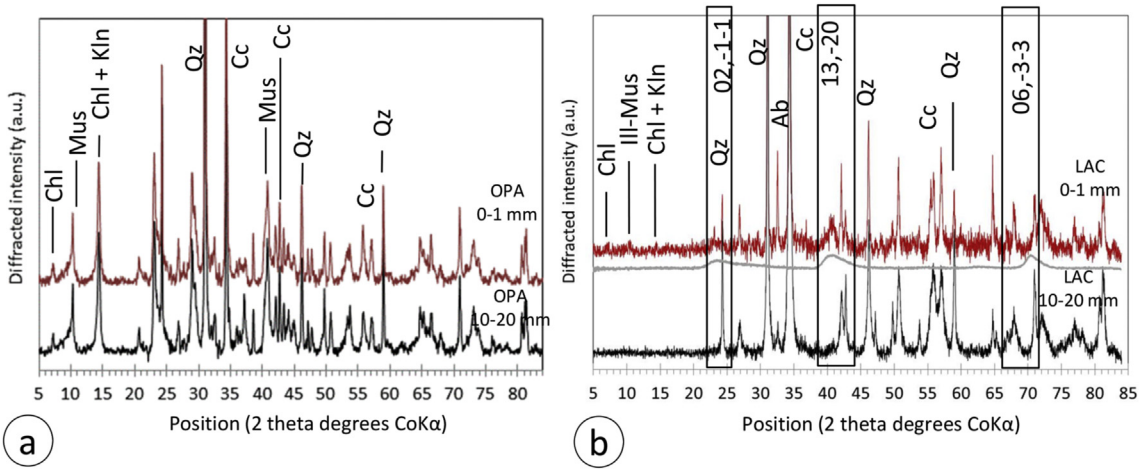

Fig. 6. XRD patterns – (a) OPA near and far from the interface; (b) LAC concrete samples far and near the interface; grey XRD pattern of synthetic M-S-H 0.6 with position of the three major peaks (Roosz et al., 2015). Mineral abbreviations used in the paper: Ab, albite; Cc, calcite; Chl, chlorite; Dol, dolomite; Kln, kaolinite; Mus, muscovite. Other abbreviations: Octa for octahedral site and Tetra for tetrahedral site.

Table 2
Mineralogical quantification in OPA using XRD; Amounts of minerals are given in weight percents. Previous mineralogical quantifications of shaly facies of OPA are given for comparison (Jenni et al., 2014; Lerouge et al., 2015; Pearson et al., 2003). The method of mineral quantification used in this work is similar to that used in Lerouge et al. (2015).

Sample	Reference OPA (Pearson et al., 2003)	Jenni et al., 2014	Lerouge et al., 2015	OPA 10–20 mm	OPA 0–1 mm	Incertainty (weight %)
Quartz	6–24	10	11–14	16	15	3
Microcline	1–3	3	1	<1	2	3
Plagioclase	1–2		2–3	2	<1	3
Calcite	5–28	20	8–22	10	13	3
Dolomite	0.2–2		0–2	1	1	3
Siderite	1–4	2	0–3	0	0	3
Kaolinite	15–33	24	15–17	14	14	5
Illite-Mica	16–40	20	25–27	28	26	5
Chlorite	4–20	8	3–4	5	5	5
Illite-Smectite	5–20	10	18–19	18	17	5
Clay fraction	58–76	62	61–67	65	62	

(24 wt% kaolinite, 20 wt% illite, 10 wt% illite/smectite mixed layers, 8 wt% chlorite), 3 wt% feldspars, 20 wt% calcite, 2 wt% siderite, 1 wt% dolomite/ankerite, 10 wt% quartz, 1 wt % pyrite, <1 wt% organic carbon.

white crust (Fig. 8 d and e). The reduced aggregate signal provides evidence in the 400-2000 cm^{-1} range of broad bands at ~1635, ~1020 and ~465 cm^{-1}, and of a high adsorption band in the 3000-4000 cm^{-1} range with a major band at ~3460 cm^{-1} with weak shoulders at ~3640, 3670–3680, and possibly at ~3700-3710 cm^{-1}. The large adsorption in the 3000-4000 cm^{-1} range indicates the presence of structural hydroxyl groups and/or water sorption. The bands at ~3670–3680, ~3640, ~1650, ~1020 and ~465 cm^{-1} fit well to maxima of synthetized M-S-H 0.6 (Roosz et al., 2015), suggesting that their structures may be similar. The normalization of the spectrum versus pure synthetized M-S-H 0.6 enabled to estimate the M-S-H content at about 25 wt % in the LAC cement in the white crust (sieved LAC 0–1 mm).

6.4. Raman spectroscopy

Raman spectra acquired on the M-S-H phase present in the white crust are reported in Fig. 8 g. In all the spectra, a high peak at ~1085 cm^{-1} associated with lower peaks or at ~712 cm^{-1} and ~281 cm^{-1} is present and is attributed to calcite (Gillet et al., 1996). Traces of quartz were detected (431 cm^{-1}). The M-S-H phase is characterized by two bands at 370 cm^{-1} and at 673 cm^{-1}. These two peaks are common with those of Raman spectrum of synthetized M-S-H 0.6 described by Roosz et al. (2015). According to Wang et al. (2002), the major peak at 673 cm^{-1} should be attributed to the vibrational modes of Si-O_b-Si bonds (O_b = bridging oxygen), which connect the SiO_4 tetrahedra that make up a layer. The peak at ~370 cm^{-1} is likely from a complex set of Mg translational movements in octahedral sites relative to the SiO_4 groups in tetrahedral layers.

6.5. ^{29}Si NMR of the Mg-Si cement phase of the white crust

The occupancies of Si bridging tetrahedra in the M-S-H phase were characterized in the same sample of white crust as that used for XRD using a high-resolution solid-state ^{29}Si NMR technique (Fig. 9). The ^{29}Si chemical shift in solid silicates is significantly impacted by the degree of polymerization Q^n of the silicon-oxygen and by the octahedral environment of the silicon nucleus, where Q represents the Si atom which is bonded to four oxygen atoms and n is related to the number of Si neighbours. Major resonances at −93.2 ppm and −85.6 ppm are assigned to Q^3 and Q^2 silicon environments, respectively. Broad resonances are compatible with a substantial amount of disorder in the Si sites. The slight shoulder near −78 ppm could be assigned to Q^1 silicon environment. In the assumption of a layered structure, this may be due to Si atoms located at the border of the particle. A slight shoulder near −105 ppm could be assigned to Q^4 silicon environment and is attributed to residual microsilica present in the initial LAC cement.

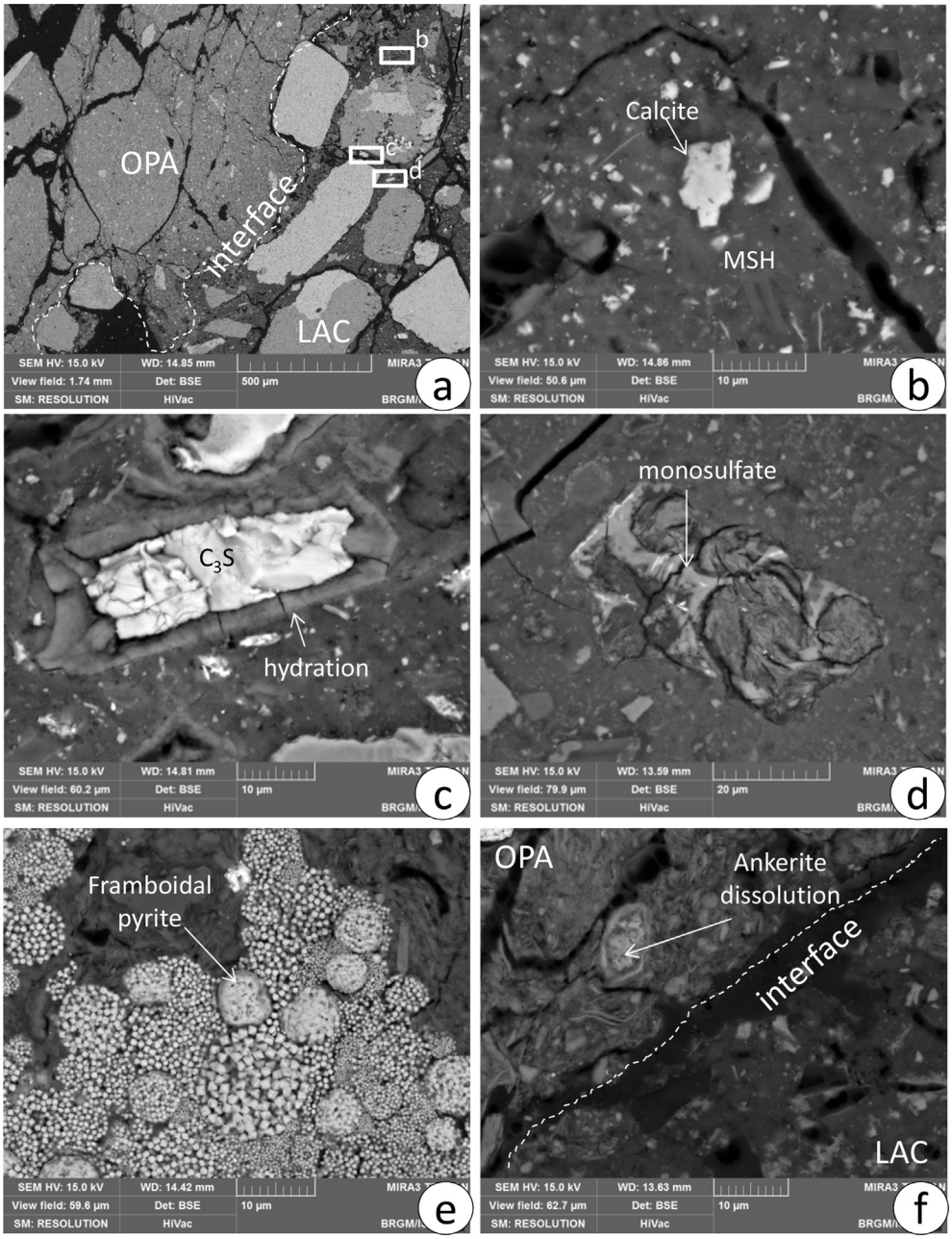

Fig. 7. BSE images of the interface– (a) general aspect; (b) matrix of M-S-H enclosing micron-sized grains of calcite in the white crust on the concrete side; (c) detail on a partially hydrated CMAS clinker (Ca-Mg-Al-Si oxides); in the white crust on the concrete side (d) detail of a partially hydrated monosulfate clinker in the white crust on the concrete side; (e) Detail of framboidal pyrite showing no oxidation on the OPA side; (f) Ankerite crystal showing altered rims suggesting dissolution on the OPA side.

6.6. Electron microprobe on the white crust

Element maps (Si, Al, Fe, K, Na, Ca, Mg, Ti, Mn, S) on the white crust in contact with OPA were processed using the µMAPphase software (Prêt et al., 2010) to display the spatial distribution of the phases over a surface area of 1 × 1 mm^2 with a resolution of 2 µm. All the pixels of the mapped area were first projected in a Si – Ca – Al_3FeMg ternary diagram in which the theoretical compositions of the main clinker phases, pozzolans, hydrates and aggregates were superimposed on the diagram to ease reading and interpretation of these chemical scatterplots (Fig. 10). The full methodology of mineral segmentation combined with macropore thresholding on the BSE images yielded the detailed phase map where each pixel is associated with mineral species or macropores (Gaboreau et al., 2012). The mineralogical mapping of the white crust allowed identifying and quantifying anhydrous phases (slag and aggregates: quartz, calcite, dolomite and plagioclase), sulfates and hydrates (dominant Ca-Al bearing M-S-H and C-A-S-H), and displaying the slag hydration process.

Quantitative profiles of Al, Ca, Mg and Si were performed through the white crust using the electron microprobe, to refine the chemical composition of the M-S-H phase (Fig. 11). Analyses indicate the systematic presence of Ca, Fe and Al in the M-S-H phase. Taking into account the nanometric size of the particles and the 1–2 µm size of the beam, it remains unclear whether these elements are incorporated in M-S-H or arise from the neighbouring

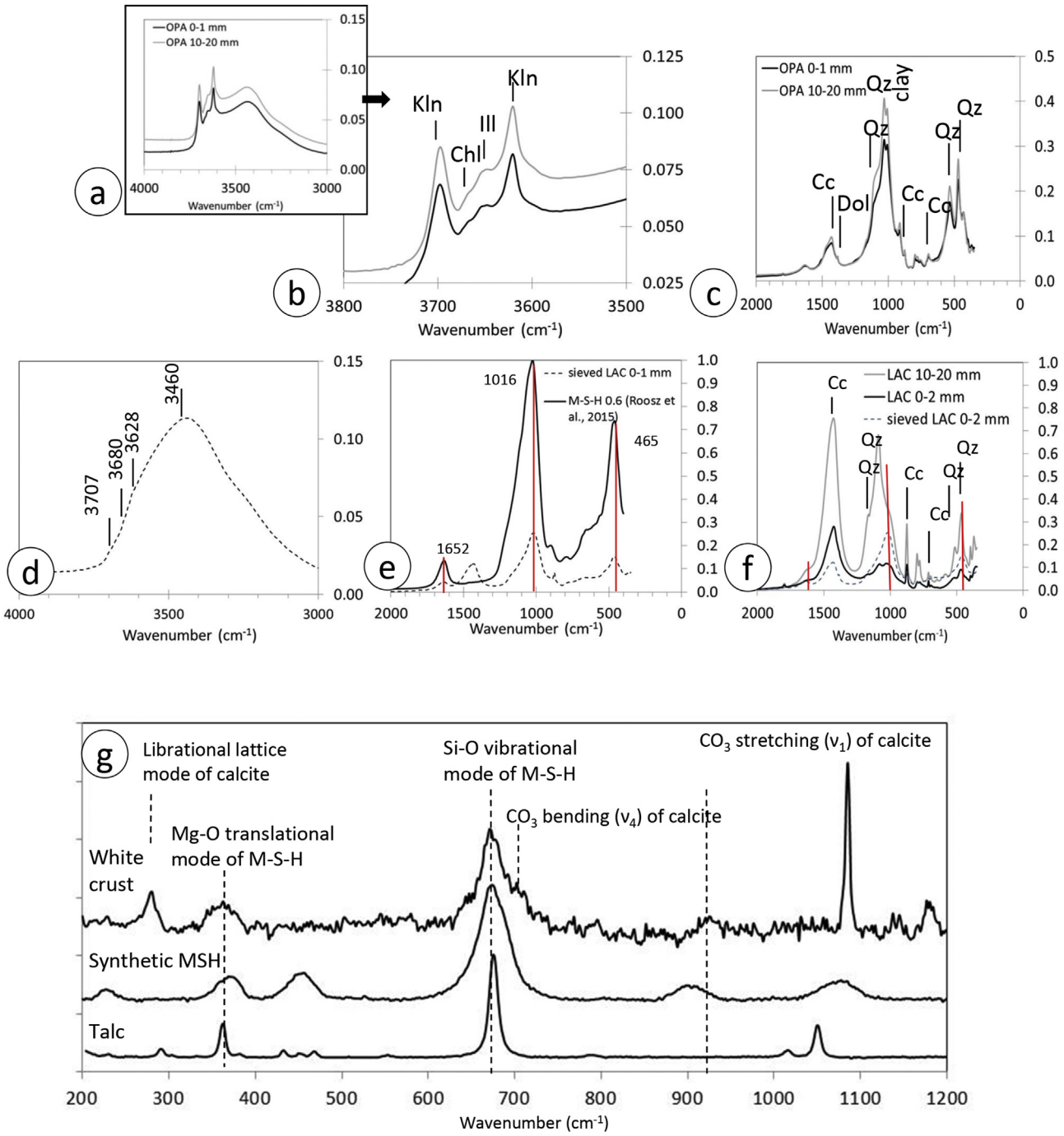

Fig. 8. Infrared and Raman spectrometry – (a) the 4000-3000 cm^{-1} zone of infrared spectrum of OPA near and far from the interface, attributed to OH vibrations; (b) detail of peaks corresponding to different clay minerals present in OPA; (c) the 2000-300 cm^{-1} zone of infrared spectrum of OPA near and far from the interface, allowing identification of quartz, calcite, dolomite; (d) the 4000-3000 cm^{-1} zone of infrared spectrum of sieved LAC 0–1 mm concrete, attributed to OH vibrations; (e) 2000-300 cm^{-1} Infrared spectra of sieved LAC 0–1 mm concrete normalized to synthetic M-S-H 0.6 (Roosz et al., 2015); (f) 2000-300 cm^{-1} infrared spectra of bulk LAC cement near and far from interface, and of a sieved fraction of the white crust normalized to calcite; (g)in situ Raman spectrum of the M-S-H at LAC/OPA interface, compared with Raman spectra of synthetic M-S-H 0.6 (Roosz et al., 2015) and natural talc from Luzenac.

cement matrix (such as calcite, silica fume, or an Al-Si cement phase).

6.7. TEM observations and analyses of white crust interface

The finely divided cement material in the white crust consists of a M-S-H phase, partially C_2S and C_3S hydrated clinkers, and a mix of C-A-S-H and amorphous silica and clay particles from OPA (Fig. 12). Clay particle size ranges between 20 and 500 nm. The particles are systematically rich in Mg, Fe and Al, with minor K and Ca. Layer-to-layer distance measurements indicate a value close to 10 Å, consistent with illite. It is noteworthy here that this illite is inherited from OPA and not neoformed.

C-S-H phases near the interface occur as aggregates of 20–50 nm-sized crystals. They have almost homogeneous chemical composition including Ca, Si, and Al, with a very low Ca/Si ratio of

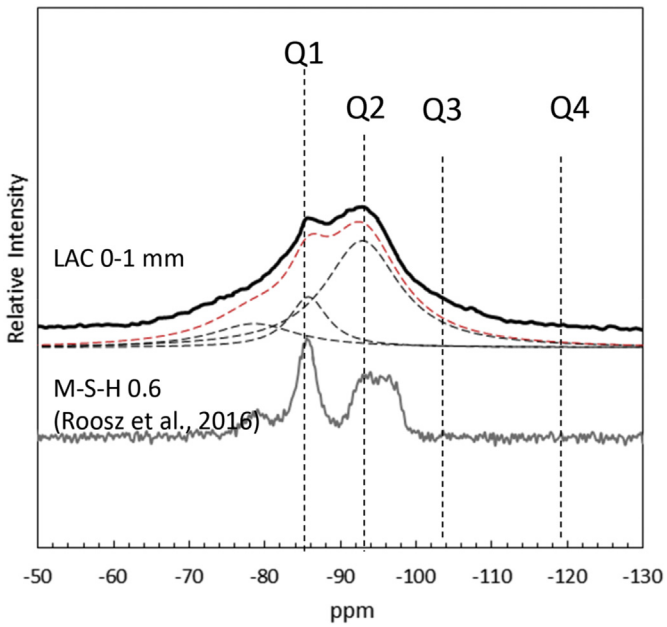

Fig. 9. ^{29}Si NMR spectrum of LAC 0–1 mm compared to those of synthetic M-S-H 0.6 (Roosz et al., 2015).

≈0.3. This low value is probably due to nanosilica contamination. The M-S-H phase always occurs as aggregates of 20–200 nm sized crystals (Fig. 13); no isolated crystals were observed. Under the beam, aggregate stability was very short.

The M-S-H phase seems to have a layered structure with particles containing on average between 2 or 3 stacked layers. The layer-to-layer distance was found to be ~14–15 Å (Fig. 13). In addition, 23 EDX analyses of aggregates indicate chemical compositions including Mg, Ca, Al, K and Si. When data are drawn in a diagram representing Mg (in at. %) as a function of Si (in at. %), they align along 1:1 straight line with a negative slope, suggesting the incorporation of Ca, Fe and Al in the phase lattice rather than phase mixing. Electron microprobe analyses of M-S-H acquired through the white crust and reported in the same diagram are consistent with the TEM analyses that contain the poorest amount (in at. %) in Mg (Fig. 13). Selected area diffraction patterns of several aggregates confirm the poorly crystalline nature of M-S-H, and the presence of only two diffraction maxima at *d*-values of ~1.6 and ~2.2 Å.

7. Discussion

7.1. Porosity changes

Porosity measurements performed near the OPA/LAC interface provide evidence for a porosity increase in both materials toward the interface. Inside OPA, the porosity increases from ~17%, consistent with previous measurements (1.5 cm from the interface) up to ~43% (0–1 mm from the interface). The fracture network displayed by the porosity map affects OPA over several centimetres with the maximum fracture density at the interface. This clearly indicates that the porosity increase may partially be related to the fracture density due to the drilling procedure during the experiment: 1) establishment of the experiment and borehole drilling previous to filling the boreholes with concrete and 2) overcorings, but also due to sawing the samples, although care was taken (Jenni et al., 2014). The absence of fracture in-fills strongly suggests that these fractures were formed during overcoring and are therefore post mortem. No conclusion can be drawn on a porosity evolution induced solely by the alkaline perturbation.

On the concrete side, porosity increase in the hydraulic binder is limited to the ~1 mm marked by the white crust. This increase is mainly due to the degradation of the concrete with the dissolution of cement grains and the precipitation of porous hydrated phases like (C-S-H or M-S-H).

7.2. Chemical changes

Elemental mapping of the interface between OPA and LAC after 5 years of interaction using micro-XRF, SEM and electron microprobe confirm that the first millimetre of concrete corresponding to the white crust is enriched in Mg, as is a ~300-500 μm-thick Mg-rich band in the OPA at ~500 μm from interface as reported by Dauzères et al. (2016) for the same interface, by Jenni et al. (2014) for this interface after 2.2 years of interaction, and for other interfaces between clayrock and low-pH cement (Dauzères, 2010; García Calvo et al., 2010; García Calvo et al., 2013). Micro-XRF also provides evidence for very high Mg content in the white crust relative to concrete and OPA, and of progressive Mg increase through the white crust toward the contact. The Mg-rich band in OPA, combined with Mg concentrations of CEC in OPA at the interface strongly suggests Mg migration from OPA to concrete. Concerning other major elements (Ca, Al, Si, and S), the white crust has a chemical composition intermediate between concrete and OPA. This data combined with probable gypsum in OPA at the interface (increase of SO_4 x 2.5 in aqueous leaching combined with Ca concentration in CEC) and slight Al depletion observed by SEM mapping in OPA both suggest that S and Al also migrate from OPA to concrete. Concerning Ca, the white crust might correspond to a zone of Ca migration from concrete to OPA; the slight Ca increase in CEC on the OPA side favours this hypothesis. These results are consistent with previous conclusions after 2.2 years of interactions (Jenni et al., 2014).

7.3. Mineralogical changes

OPA clay mineralogy remains largely unmodified, according to bulk XRD patterns and IR spectra. Mineralogy of the clay fraction and proportions of clay minerals remain unchanged near the interface; this is consistent with the almost homogeneous CEC measurements. Calcite content remains almost unchanged, which is consistent with the limited pH increase due to the low alkaline content of the LAC concrete. Ankerite is the only phase that seems to present signs of dissolution that might be due to oxidation rather than pH change. The presence of a sulfate-phase is suspected in OPA at the interface (OPA 0–1 mm), according to both CEC and aqueous leaching data. Note that chemical and mineralogical changes in OPA near the interface with LAC concrete are at the limit or below the accuracy of most of the techniques we used.

As for the concrete, mineralogy significantly changes at the interface with OPA and is marked by the formation of the <1 mm thick Mg-rich white crust and extensive cracks. According to Dauzères et al. (2016) and Nied et al. (2016), the Ca/Si ratio is very low. Ca is leached and the C-S-H signal is absent in the white crust. In this study, micro-XRF data rather suggest that the white is a result of interaction between LAC concrete and OPA, characterized by an intermediate composition between that of concrete and OPA, except for high Mg content.

Mineral quantification using electron microprobe mapping, IR spectroscopy, XRD patterns, and SEM observations provides evidence of quartz, calcite and dolomite aggregates cemented by a mix of a M-S-H phase with a phyllosilicate-like structure, micron-grained calcite, C-S-H, and partially hydrated clinkers; portlandite is absent. Complementary TEM observation of microtome sections

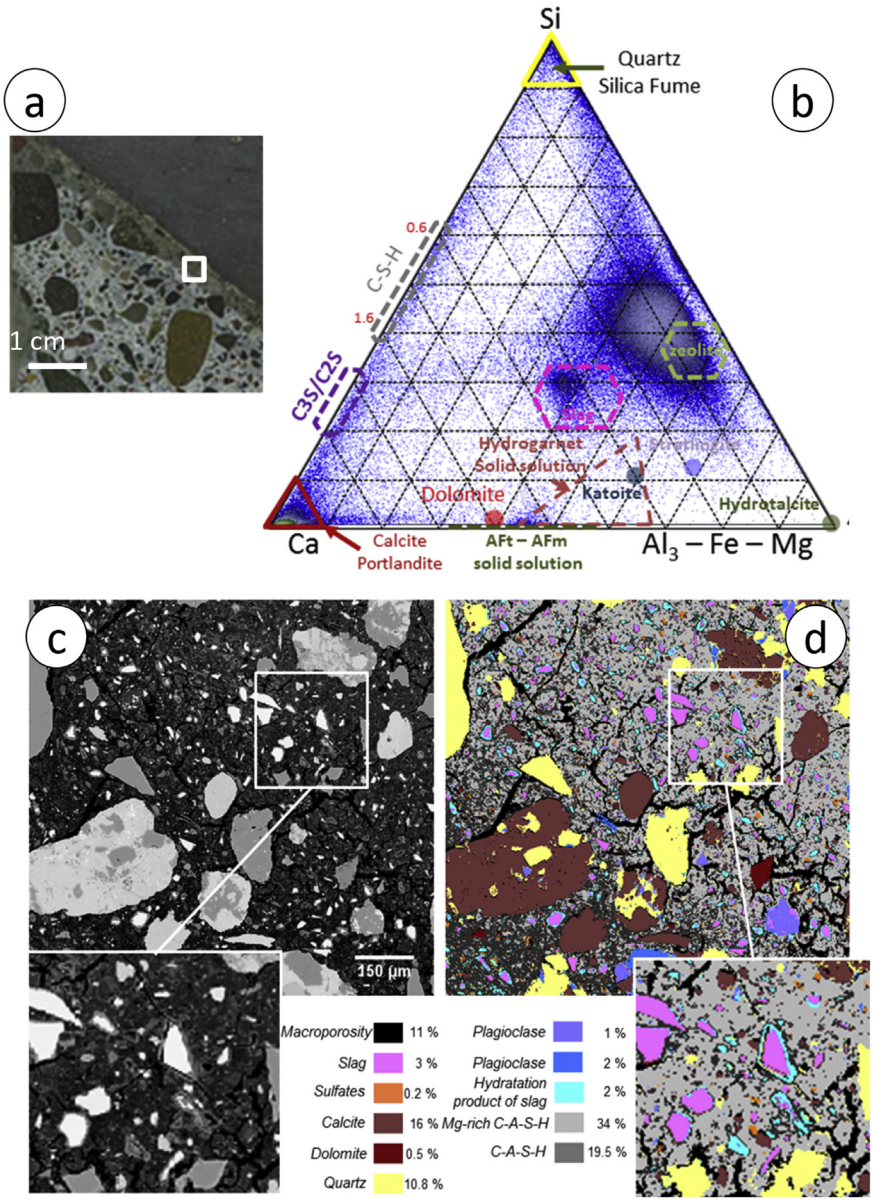

Fig. 10. EPMA mineral quantification - (a) Polished section of the interface; (b) Si – Ca – Al_3FeMg ternary projection of all the pixels of the mapped area. The main aggregates, pozzolan and hydrates of a hardened cement material end members are indicated; (c) Back-scattered electron image of the mapped area; (d) Mineral map of the same area.

of sieved white crust identifies rare detrital clay particles coming from OPA and entrapped in the cement paste during the concrete emplacement. The cement paste consists of aggregates of 20–50 nm-sized C-S-H crystals with a low Ca/Si ratio of ~0.3, micron-sized calcite and M-S-H. Coexistence of M-S-H and C-S-H was already described by Brew and Glasser (2005). C-S-H have Ca/Si ratios generally reported to vary between 0.6 and 2.4 (Grangeon et al., 2013), strongly suggesting that C-S-H with Ca/Si of ~0.3 are a fine mix of C-S-H (Ca/Si of ~0.6) and nanosilica. EPMA and EDX analyses by TEM of M-S-H indicate that the M-S-H phase also includes significant amounts of Al and Ca. The combined data indicate that the Ca content of the white crust is lower than the LAC cement paste, but this decrease is largely due to Al and Mg increases. Major elements including Ca, Mg and Al are differently distributed in the white crust than in the LAC concrete, probably due to pH differences. In the white crust, the Ca-bearing phases are calcite, Ca-Al-bearing M-S-H and C-S-H with low Ca/Si ratio. The M-S-H is the major Al- and Mg-bearing phase (approximately 25 wt % of the cement paste). By comparison, LAC concrete reactivity with clayrock is marked by disappearance of portlandite, the formation of M-S-H, low Ca/Si C-S-H and minor calcite, whereas Portland cement reactivity is dominantly characterized by disappearance of portlandite, cement carbonation and formation of low Ca/Si ratio C-S-H (Gaboreau et al., 2012).

7.4. Characterization of the M-S-H phase

Previous work on interfaces between clay and low pH cements provides evidence of the formation of M-S-H that exhibits a gel-like structure (Brew and Glasser, 2005; Dauzères et al., 2016) and could consist of talc-like precursors (Lothenbach et al., 2015), with little or no Al (Dauzères et al., 2016; Jenni et al., 2014; Nied et al., 2016). Experiments on C-S-H and M-S-H stability demonstrate that there is no solid solution between the two phases (Brew and Glasser,

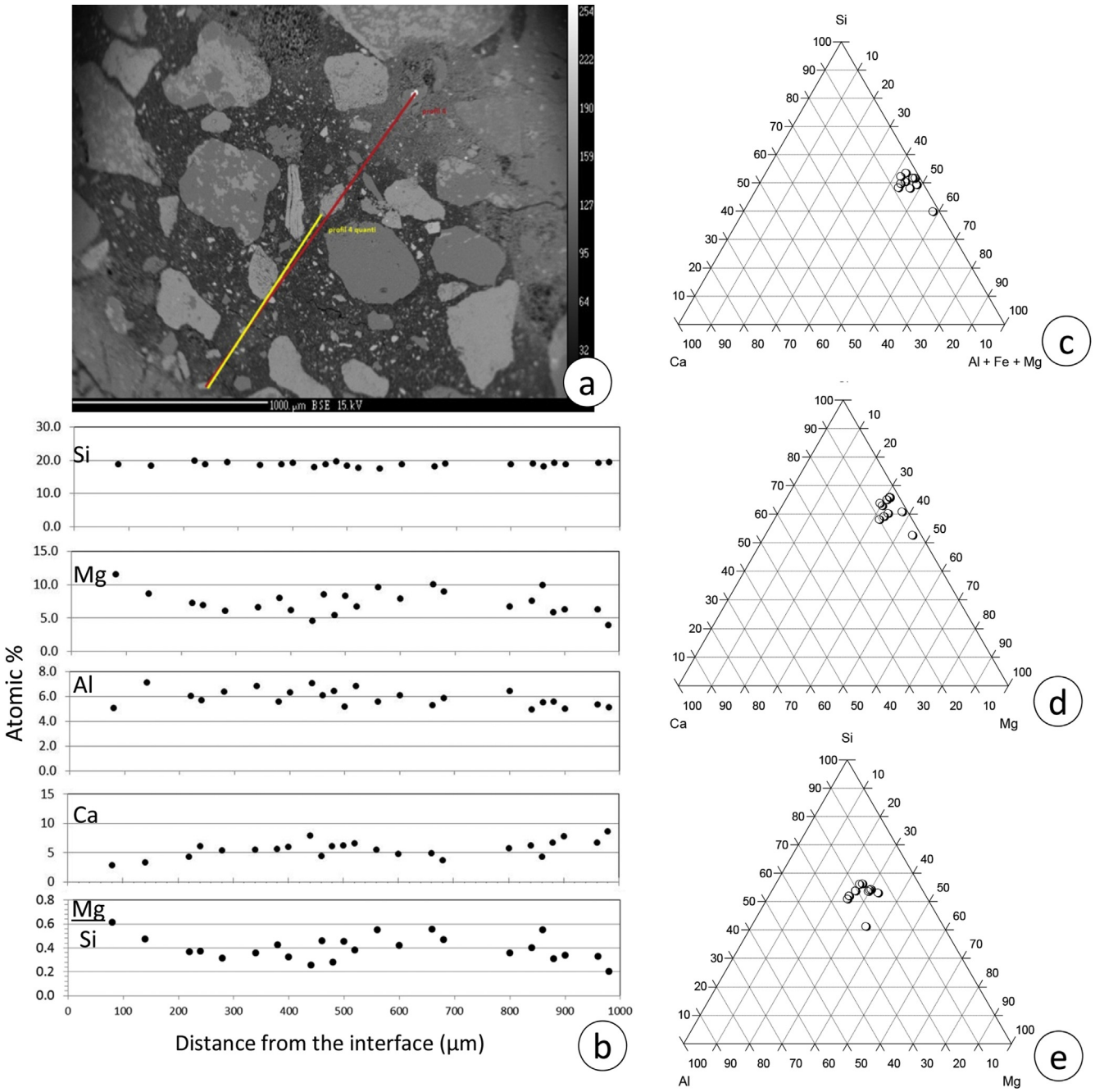

Fig. 11. Profile of EPMA analyses of M-S-H phase through the white crust in LAC concrete at interface – (a) BSE image and profile; (b) Si, Mg, Al, Ca and Mg/Si ratio of M-S-H phase; (c) Analyses reported in Ca – Si - Al + Mg + Fe ternary diagram; (d) Analyses reported in Ca – Si - Mg ternary diagram; (e) Analyses reported in Al – Si - Mg ternary diagram.

2005), but C-S-H may contain small amounts of Mg and M-S-H small amounts of Ca (Lothenbach et al., 2015). In this study, when combined, the 12 electron microprobe and 23 EDX-TEM analyses of M-S-H formed at the OPA and LAC interface indicate that M-S-H contains significant amounts of Al and Ca that need to be taken into account in its structure.

XRD, Raman, IR and ^{29}Si NMR data obtained on the M-S-H of the LAC concrete/OPA interface show numerous similarities with synthetic pure M-S-H that has a disordered talc-like structure (Roosz et al., 2015; Lothenbach et al., 2015), i.e. a tri-octahedral 2:1 phyllosilicate. However, M-S-H contains Al and Mg whereas the structure of talc consists of an octahedral MgO layer between two tetrahedral silicate sheets and does not incorporate significant amounts of Al (Martin et al., 1999). Moreover, by comparing infrared data with a natural talc spectrum, major peaks at ~1020 and ~465 cm^{-1} are enlarged, the peak at ~690 cm^{-1} occurs as a shoulder of the peak at 465 cm^{-1}, due to disordered structure, and the sorption in the 3000-4000 cm^{-1} range is stronger than those of talc, probably due to the presence of interlayer water. The approximate spacing measured by TEM (~14-15 Å), electron diffraction and IR spectra are compatible with smectite (Brown and Brindley, 1984; Baldermann et al., 2014), vermiculite (Farmer and Russell, 1964) or swelling chlorite (Brown and Brindley, 1984).

Therefore, the structural properties of the M-S-H phase seem to be consistent with a 2:1 phyllosilicate, with Al-Si substitution in tetrahedral sites, and Al-Mg substitution in octahedral sites. These

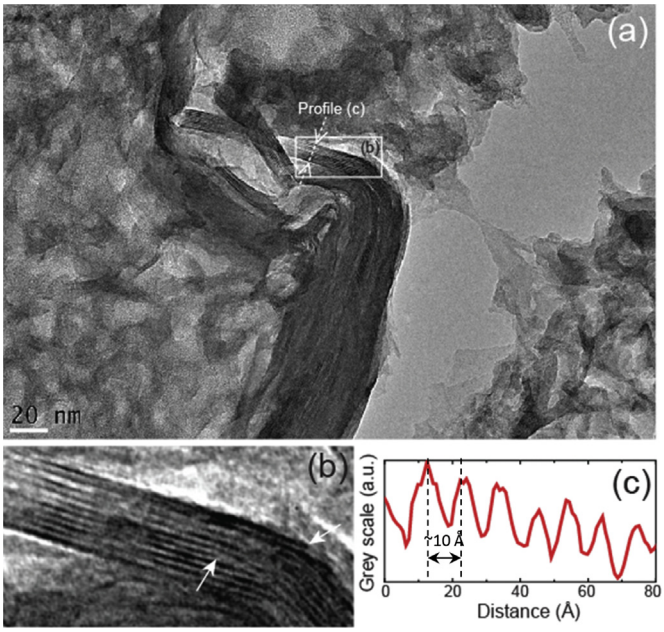

Fig. 12. TEM observation of clay particle from OPA enclosed in the white crust (a) Raw TEM image of a layered material suffering from visible bending and aggregation. (b) Fourier-filtered part of the image (squared area in a) revealing the presence of many dislocations, the most obvious being pointed out with arrows (c) Layer-to-layer distance, estimated at ~10 Å from a grey scale profile taken perpendicular to the layer plane in the raw image.

Al substitutions create layers with negatively charged surfaces compensated by a supplementary cationic layer in interlayer spaces. The cationic layer consists of cations in vermiculite or smectite, and of a brucitic layer in chlorite. Based on this hypothesis, we have used a stepwise approach to calculate an average structural formula.

Firstly, structural formulae of the 23 EDX analyses combined with TEM and the 12 EPMA analyses were calculated on the basis of the structure of a 2:1 phyllosilicate with four tetrahedral sites and an interlayer charge, assuming:

- that Al was preferentially tetrahedral, the rest being in the octahedral sites,
- that Fe is Fe^{3+} in octahedral sites,
- that Mg is preferentially in the octahedral sites,
- that Ca is in the interlayer,
- that the charge is compensated by the rest but cannot exceed the layer charge.

For the 13 EDX analyses, called MET population 1 in the following text, and for the 12 EPMA analyses, the sum of Mg^{2+}, Fe^{3+}, and Al^{3+} in octahedral site ranges between 2 and 3. These analyses reported in a Si^{4+} versus R^{2+} diagram (Meunier, 2003) are distributed between the field of dioctahedral and trioctahedral 2:1 phyllosilicates (Fig. 14). The Si enrichment of most EPMA data relative to the ditrioctahedral field may be attributed to nanosilica contribution, due to the μm-size of the beam, which is larger than the 20–50 nm size of the M-S-H particles, in comparison with TEM, which has higher spatial resolution.

Based on the above-mentioned hypothesis and considering that a 2:1 phyllosilicate general formula (Meunier, 2003) is:

$(Ca, Mg)^{(x-y+2z)+}$ $[(Mg_{3-y-z}, R^{3+}{}_y, \square_z)$ (Al_x, Si_{4-x}) O_{10} $(OH)_2]$ $^{(x-y+2z)-}$, where □ is a vacant site, and R^{3+} are trivalent cations such as Al and Fe, the derived average formula are the following:

$(Ca_{0.5\pm0.2})$ $(Mg_{2.0\pm0.4}, Fe_{0.2\pm0.1}, Al_{0.5\pm0.3}, \square_{0.3\pm0.3})$ $(Al_{0.9\pm0.2}, Si_{3.1\pm0.2})$ O_{10} $(OH)_2$, based on TEM measurements.

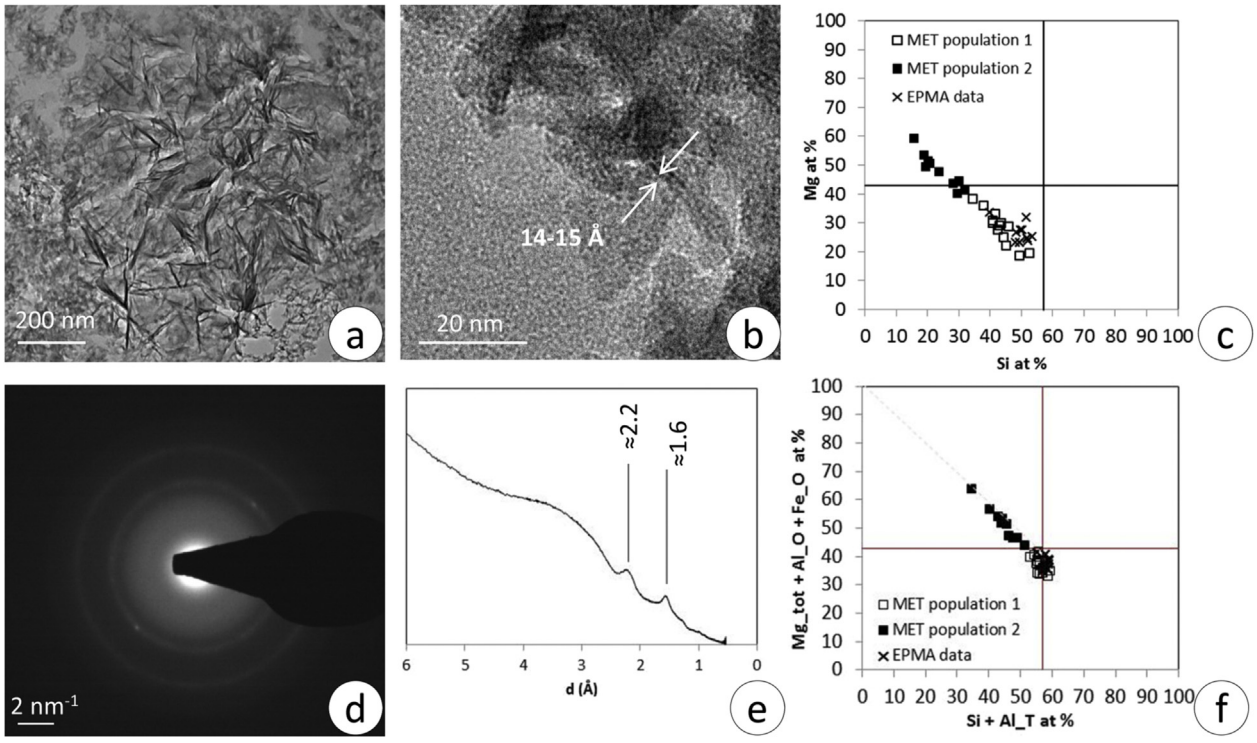

Fig. 13. Observation of M-S-H by TEM – (a) image of an aggregate of M-S-H particles; (b) Layer-to-layer distance estimated at 14–15 Å; (c) EDX and EPMA analyses of M-S-H reported in a Mg-Si diagram. The lines correspond to theoretical Mg and Si compositions of tri-octahedral 2:1 phyllosilicate $[Mg_3Si_4O_{10}(OH)_2]$; (d) electron diffraction of the aggregate of image a; (e) Selected area electron diffraction pattern; (f) EDX and EPMA analyses of M-S-H reported in a Mg + Al_{Octa} + Fe versus Si + Al_{Tetra} diagram.

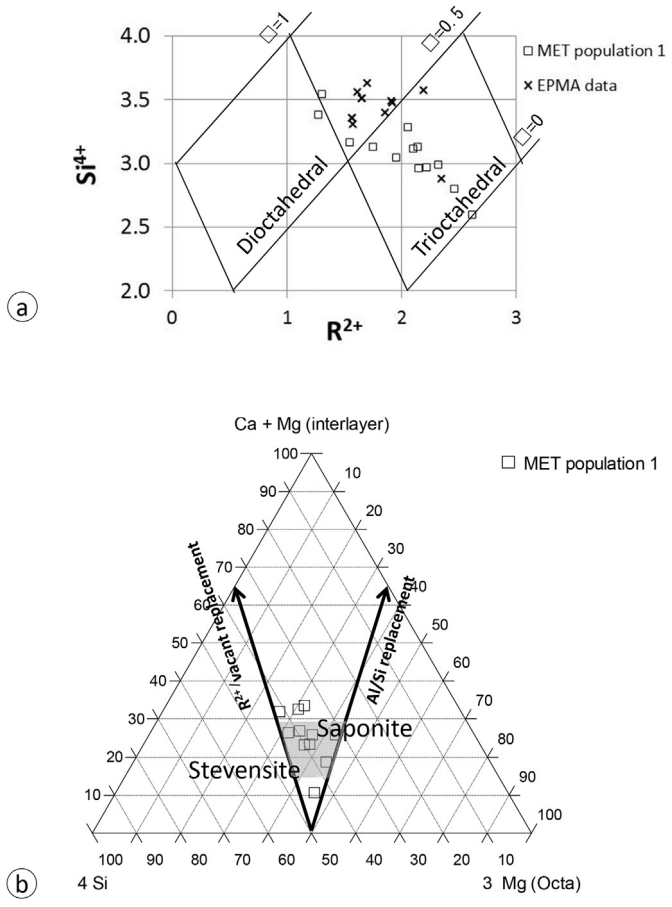

Fig. 14. (a) EDX and EPMA analyses of M-S-H reported in a Si versus R^{2+}diagram showing the field of di-octahedral and trio-octahedral phyllosilicates, according to Wiewiora and Weiss (1990); (b) EDX analyses reported in a 4 Si − Ca + Mg − 3 R2+ ternary diagram showing the field of tri-octahedral phyllosilicates such as saponite and stevensite (Meunier, 2003).

$(Ca_{0.3\pm0.2})$ $(Mg_{1.8\pm0.3}, Fe_{0.1\pm0.1}, Al_{0.7\pm0.2}, \square_{0.4\pm0.2})3(Al_{0.6\pm0.2}, Si_{3.4\pm0.2})$ O_{10} $(OH)_2$, based on EPMA measurements.

The two average structural formulas obtained from two different analytical techniques, TEM and EPMA, at two different scales, are almost consistent, except for the slightly higher Si content in EPMA analyses as already discussed before. When EDX analyses are plotted in a 4 Si^{4+}- charge − 3 R^{2+} diagram (Meunier, 2003), M-S-H data plot in the saponite field (Fig. 14).

For the remaining 10 EDX analyses (MET population 2), even though the 3 octahedra are filled, the residual Mg in the interlayer space is high, and the charge of the interlayer space is significantly higher than the negative charge of the 2:1 layers:

$(Ca_{0.3\pm0.1}, Mg_{1.7\pm1.1})$ $(Mg_{2.7\pm0.3}, Fe_{0.3\pm0.2})$ $(Al_{1.9\pm0.3}, Si_{2.1\pm0.3})$ O_{10} $(OH)_2$

Various assumptions can be considered to solve the problem of high charge in the interlayer, such as (i)the M-S-H mixing with a Mg-bearing phase as described above, and (ii) the presence of Mg as brucite $[Mg(OH)_2]$ in the interlayer and the formation of a chlorite phase precursor.

7.5. Comparison with OPC/claystone interfaces – constraints on low-alkali concrete/claystone interactions and modeling

Interactions between OPC concrete and clayrocks are limited to the few millimeters in concrete, marked by high carbonation and formation of low Ca/Si ratio C-S-H, and dominated by a chemical perturbation of the cation exchange capacity in the first few centimeters of the clayrock (Gaboreau et al., 2011, 2012; Jenni et al., 2014; Mäder et al., 2017; Tinseau et al., 2006). The sorption capacity of clayrock does not significantly change, but the cation distribution on the exchanger is generally marked by an increase of K at the expense of Mg (Gaboreau et al., 2011, 2012; Jenni et al., 2014; Mäder et al., 2017). These major changes due to the high pH contrast are consistent with a diffusion of alkali-metal (no mineral control in the cement) and Ca^{2+} ions (portlandite dissolution) from cement to clay and with a diffusion of Si, Mg, Al (dissolution of phyllosilicate) from clay to cement.

The addition of slag and nanosilica to OPC is used to reduce the alkali content and achieve concrete pore waters with a pH of 10–11, that are more compatible with the pH of clay environment (García Calvo et al., 2010 García Calvo et al., 2013; Lothenbach et al., 2012, 2014). In the case of LAC cement, the pH of pore water solution was 12.3 ± 1.0 (Lothenbach et al., 2012). The pH of OPA pore water at Mont Terri was measured to be 7.1 ± 0.4 (Vinsot et al., 2008) and modeled to be 7.3–7.8 (Pearson et al., 2011). The volumes of materials impacted by interactions between LAC concrete and clayrocks do not seem very different from those observed at OPC/Clay interfaces. Within the first millimetre of the LAC concrete that is in contact with OPA, a white crust can be found which is formed of a (Ca, Mg) smectite-type clay mineral, low Ca/Si ratio C-S-H and minor calcite. The formation of this white crust was not observed in the OPC-OPA. On the clay side, the cation distribution of the clay exchanger is modified in the first centimeters of clayrock near interface; but in case of the LAC/OPA interface the increase of K charge is lower than in the case of OPC/clay interface, while Mg is less depleted and even increases at the LAC/OPA interface. Assuming that Al, Mg and Si result from the dissolution of phyllosilicates, as described for OPC/clay interactions, a lower Mg depletion on the clay side should indicate a lower dissolution of phyllosilicates in clayrocks in contact with LAC concrete than in clayrocks in contact with OPC concrete. However, the precipitation of (Ca, Mg) smectite at LAC interface and chemical changes suggest that the diffusion of Si, Al and Mg remains from clay to concrete. It must be noted that the contribution of Mg and Al from slags cannot be neglected, according to hydration study of the LAC cement (Lothenbach et al., 2012).

In this study, (Ca, Mg) smectite is probably for the first time identified at the interface between natural clayrock and cementitious material. Previously, the presence of (Ca, Mg) smectite was predicted by numerical modeling of OPC concrete/clay interactions (Gaucher et al., 2004; Marty et al., 2015; Savage, 2014a; Trotignon et al., 2007) and by modeling of iron/steel-bentonite interactions (Savage, 2014b), and was identified in experimental interactions between FEBEX bentonite (Spain) and OPC cement porewaters (Cuevas, 2004; Sánchez et al., 2006). The pH of a pore solution at equilibrium with mineral phases of the white crust including C-S-H 0.8, (Ca, Mg) smectite, calcite and amorphous silica was calculated at 10.3 using the PHREEQC (version 2.18) software and the THERMODDEM thermodynamic database (version 2011). This pH is in the range of pH expected between clayrock and cementitious material. The (Ca, Mg) smectite formation might also be interpreted as the result of attenuated interaction between both materials, and rather indicates a relative continuity of the sorption capacities of the materials at the concrete/clayrock interface.

8. Conclusions

Studies of interfaces between low pH concrete and claystone are scarce in comparison to the number of studies on Portland cement-clay interactions. The long-term Cement-Clay interaction (CI) experimental program at the Mont Terri Rock Laboratory (St.

Ursanne, Switzerland) has provided an opportunity to characterize interactions between low pH concrete (LAC) and OPA Clay after five years, in terms of chemical, mineralogical and petrophysical changes.

In the OPA, perturbation is marked by an increase of porosity probably due to drilling and sawing artefacts and by chemical changes marked by a 300–500 μm thick Mg-rich band at 500 μm of the interface associated with increased Mg^{2+} cations in the clay exchanger, and by a slight SO_4 increase due to slight pyrite oxidation. In the LAC concrete, perturbation is marked by increased porosity, Mg enrichment combined with slight Ca and S depletion, and formation of a white zone that contains (Ca, Mg smectite), a low Ca/Si ratio C-S-H and calcite. Combined electron microprobe and EDX analyses using TEM indicate that the (Ca, Mg) smectite is a ditrioctahedral 2:1 phyllosilicate with a chemical composition of $(Ca_{0.5\pm0.2})$ $(Mg_{2.0\pm0.4}, Fe_{0.2\pm0.1}, Al_{0.5\pm0.3}, \square_{0.3\pm0.3})$ $(Al_{0.9\pm0.2}, Si_{3.1\pm0.2})$ O_{10} $(OH)_2$.

The formation of smectite is in agreement with predictive modeling of interactions between concrete and clay (Gaucher et al., 2004; Marty et al., 2015; Savage, 2014a; Trotignon et al., 2007). For the analyses with the highest Mg content, the charge balance is highly positive due to this Mg. It may be present in the interlayer space as $Mg(OH)_2$.

Acknowledgements

This research has been financially supported by the partners of the Mont Terri Consortium participating in the CI Experiment (ANDRA, CRIEPI, FANC, Nagra, Obayashi, and SCK CEN) and the BRGM Research. We thank Cédric Duee, Nicolas Maubec, Stéphane Touzelet, Guillaume Wille from BRGM and Valérie Montouillout from CNRS-CEMHTI (Orléans) for their analytical support. We are grateful to Dr Karen M. Tkaczyk (McMillan translation) for proofreading and editing the English text. The associate editor, Dr Eric Wieland and the two anonymous referees are thanked for their constructive comments and the improvement of the manuscript.

Appendix A. Supplementary data

Supplementary data related to this article can be found at http://dx.doi.org/10.1016/j.pce.2017.01.005.

References

Adler, M., Mader, U.K., Waber, H.N., 1999. High-pH alteration of argillaceous rocks: an experimental study. Schweiz. Mineral. Und Petrogr. Mittl. 79, 445–454.
Alonso, M.C., García Calvo, J.L., Hidalgo, A., Fernández Luco, L., 2010. 10-Development and application of low-pH concretes for structural purposes in geological repository systems. In: Ahn, J., Apted, M.J. (Eds.), Geological Repository Systems for Safe Disposal of Spent Nuclear Fuels and Radioactive Waste. Woodhead Publishing, pp. 286–322.
Andra, 2005. Dossier 2005 Argile: Evaluation de la faisabilité du stockage géologique en formation argileuse profonde, Rapport de synthèse. Andra, France. http://www.andra.fr.
Apted, M., Ahn, J., 2010. Multiple-barrier geological repository design and operation strategies for safe disposal of radioactive materials. In: Ahn, J., Apted, M.J. (Eds.), Geological Repository Systems for Safe Disposal of Spent Nuclear Fuels and Radioactive Waste. Woodhead Publishing, pp. 3–28.
Baldermann, A., Dohrmann, R., Kaufhold, S., Nickel, C., Letofsky-Papst, I., Dietzel, M., 2014. The Fe-Mg-saponite solid solution series – a hydrothermal synthesis study. Clay Miner. 49, 391–415.
Bartier, D., Techer, I., Dauzères, A., Boulvais, P., Blanc-Valleron, M.M., Cabrera, J., 2013. In situ investigations and reactive transport modelling of cement paste/argillite interactions in a saturated context and outside an excavated disturbed zone. Appl. Geochem. 31, 94–108.
Bauer, A., Berger, G., 1998. Kaolinite and smectite dissolution rate in high molar KOH solutions at 35°C and 80°C. Appl. Geochem. 13, 905–916.
Bérubé, M.-A., Choquette, M., Locat, J., 1990. Effects of lime on common soil and rock forming minerals. Appl. Clay Sci. 5, 145–163.
Berner, U.R., 1992. Evolution of pore water chemistry during degradation of cement in a radioactive waste repository environment. Waste Manag. 12, 201–219.
Bildstein, O., Claret, F., 2015. Chapter 5-stability of clay barriers under chemical perturbations. In: Christophe Tournassat, C.I.S.I.C.B., Bergaya, F. (Eds.), Developments in Clay Science. Elsevier, pp. 155–188.
Brew, D.R.M., Glasser, F.P., 2005. Synthesis and characterisation of magnesium silicate hydrate gels. Cem. Concr. Res. 35, 85–98.
Brown, G., Brindley, G.W., 1984. Sample preparation methods and instrumental conditions for X-ray diffraction analysis of clay. In: Brindley, G.W., Brown, G. (Eds.), Crystal Structures of Clay Minerals and Their X-ray Identification. Mineralogical Society, London.
Chapman, N., Hooper, A., 2012. The disposal of radioactive wastes underground. Proc. Geol. Assoc. 123, 46–63.
Chen, W., Liu, J., Brue, F., Skoczylas, F., Davy, C.A., Bourbon, X., Talandier, J., 2012. Water retention and gas relative permeability of two industrial concretes. Cem. Concr. Res. 42, 1001–1013.
Codina, M., Cau-dit-Coumes, C., Le Bescop, P., Verdier, J., Ollivier, J.P., 2008. Design and characterization of low-heat and low-alkalinity cements. Cem. Concr. Res. 38, 437–448.
Cuevas, J., 2004. Geochemical reactions between the FEBEX bentonite and Portland type cement porewater. In: Michau, N. (Ed.), ECOCLAY II: Effect of Cement on Clay Barrier Performance Phase II. Final Report. European Commission. FIKWCT-2000-0028.
Dauzères, A., 2010. Etude expérimentale et modélisation des mécanismes physico-chimiques des interactions béton-argile dans le contexte du stockage géologique des déchets radioactifs. PhD thesis. University of Poitiers, France.
Dauzères, A., Achiedo, G., Nied, D., Bernard, E., Alahrache, S., Lothenbach, B., 2016. Magnesium perturbation in low-pH concretes placed in clayey environment—solid characterizations and modeling. Cem. Concr. Res. 79, 137–150.
Dauzères, A., Le Bescop, P., Cau-Dit-Coumes, C., Brunet, F., Bourbon, X., Timonen, J., Voutilainen, M., Chomat, L., Sardini, P., 2014. On the physico-chemical evolution of low-pH and CEM I cement pastes interacting with Callovo-Oxfordian pore water under its in situ CO2 partial pressure. Cem. Concr. Res. 58, 76–88.
De Windt, L., Marsal, F., Tinseau, E., Pellegrini, D., 2008. Reactive transport modeling of geochemical interactions at a concrete/argillite interface, Tournemire site (France). Phys. Chem. Earth 33, S295–S305.
Debure, M., De Windt, L., Frugier, P., Gin, S., Vieillard, P., 2016. Mineralogy and thermodynamic properties of magnesium phyllosilicates formed during the alteration of a simplified nuclear glass. J. Nucl. Mater. 475, 255–265.
Devol-Brown, I., Tinseau, E., Bartier, D., Mifsud, A., Stammose, D., 2007. Interaction of Tournemire argillite (Aveyron, France) with hyperalkaline fluids: batch experiments performed with powdered and/or compact materials. Phys. Chem. Earth, Parts A/B/C 32, 320–333.
Eberl, D.D., Velde, B., Mc Cormick, T., 1993. Synthesis of illite-smectite from smectite at Earth surface temperatures and high pH. Clay Miner. 28, 49–60.
Farmer, V.C., Russell, J.D., 1964. The infra-red spectra of layer silicates. Spectrochim. Acta 20, 1149–1173.
Gaboreau, S., Prêt, D., Tinseau, E., Claret, F., Pellegrini, D., Stammose, D., 2011. 15 years of in situ cement–argillite interaction from Tournemire URL: characterisation of the multi-scale spatial heterogeneities of pore space evolution. Appl. Geochem. 26, 2159–2171.
Gaboreau, S., Lerouge, C., Dewonck, S., Linard, Y., Bourbon, X., Fialips, C.I., Mazurier, A., Prêt, D., Bosrchenck, D., Montouillout, V., Gaucher, E.C., Claret, F., 2012. In-situ interaction of cement paste and shotcrete with claystones in a deep disposal context. Am. J. Sci. 312, 314–356.
Galle, C., 2001. Effect of drying on cement-based materials pore structure as identified by mercury intrusion porosimetry - a comparative study between oven-, vacuum-, and freeze-drying. Cem. Concr. Res. 31, 1467–1477.
García Calvo, J.L., Hidalgo, A., Alonso, C., Fernández Luco, L., 2010. Development of low-pH cementitious materials for HLRW repositories: resistance against ground waters aggression. Cem. Concr. Res. 40, 1290–1297.
García Calvo, J.L., Alonso, M.C., Hidalgo, A., Fernández Luco, L., Flor-Laguna, V., 2013. Development of low-pH cementitious materials based on CAC for HLW repositories: long-term hydration and resistance against groundwater aggression. Cem. Concr. Res. 51, 67–77.
Gaucher, E., Robelin, C., Matray, J.M., Negrel, G., Gros, Y., Heitz, J.F., Vinsot, A., Rebours, H., Cassagnabere, A., Bouchet, A., 2004. ANDRA underground research laboratory: interpretation of the mineralogical and geochemical data acquired in the Callovian-Oxfordian formation by investigative drilling. Phys. Chem. Earth 29, 55–77.
Gaucher, E.C., Blanc, P., Bardot, F., Braibant, G., Buschaert, S., Crouzet, C., Gautier, A., Girard, J.P., Jacquot, E., Lassin, A., Negrel, G., Tournassat, C., Vinsot, A., Altmann, S., 2006. Modelling the pore water chemistry of the Callovian-Oxfordian formation at a regional scale. Comptes Rendus Geosci. 338, 917–930.
Gillet, P., McMillan, P., Schott, J., Badro, J., Grzechnik, A., 1996. Thermodynamic properties and isotopic fractionation of calcite from vibrational spectroscopy of 18O-substituted calcite. Geochimica Cosmochimica Acta 60, 3471–3485.
Gin, S., Jollivet, P., Fournier, M., Angeli, F., Frugier, P., Charpentier, T., 2015. Origin and consequences of silicate glass passivation by surface layers. Nat. Commun. 6, 6360.
Goldstein, J.I., 1992. Electron probe microanalysis – electron specimen interaction. UW- Madison Geosci. 777.
Grangeon, S., Claret, F., Linard, Y., Chiaberge, C., 2013. X-ray diffraction: a powerful tool to probe and understand the structure of nanocrystalline calcium silicate hydrates. Acta Crystallogr. Sect. B-Struct. Sci. B69, 465–473.
Hellmuth, K.H., Siitari-Kauppi, M., Lindberg, A., 1993. Study of porosity and migration pathways in crystalline rock by impregnation with 14C-

polymethylmethacrylate. J. Contam. Hydrol. 13, 403–418.
Huertas, F., Fuentes-Cantillana, J.L., Jullien, F., Rivas, P., Linares, J., Fariña, P., Ghoreychi, M., Jockwer, N., Kickmaier, W., Martínez, M.A., Samper, J., Alonso, E., Elorza, F.J., 2000. Full-scale Engineered Barriers Experiment for a Deep Geological Repository for High-level Radioactive Waste in Crystalline Host Rock (FEBEX Project). European Commission, Brussels. EUR 19147EN.
Jenni, A., Mäder, U., Lerouge, C., Gaboreau, S., Schwyn, B., 2014. In situ interaction between different concretes and Opalinus Clay. Phys. Chem. Earth, Parts A/B/C 70–71, 71–83.
King, F., Shoesmith, D.W., 2010. Nuclear waste canister materials, corrosion behaviour and long-term performance in geological repository systems. In: Ahn, J., Apted, M.J. (Eds.), Geological Repository Systems for Safe Disposal of Spent Nuclear Fuels and Radioactive Waste. Woodhead Publishing, pp. 379–420.
Lerouge, C., Maubec, N., Wille, G., Flehoc, C., 2015. GD Experiment: Geochemical Data Experiment. Analysis of Carbonate Fraction in Opalinus Clay Mont Terri Project, Switzerland. Technical Note TN-2014-92.
Lothenbach, B., Le Saout, G., Ben Haha, M., Figi, R., Wieland, E., 2012. Hydration of a low-alkali CEM III/B–SiO2 cement (LAC). Cem. Concr. Res. 42, 410–423.
Lothenbach, B., Rentsch, D., Wieland, E., 2014. Hydration of a silica fume blended low-alkali shotcrete cement. Phys. Chem. Earth, Parts A/B/C 70–71, 3–16.
Lothenbach, B., Nied, D., L'Hôpital, E., Achiedo, G., Dauzères, A., 2015. Magnesium and calcium silicate hydrates. Cem. Concr. Res. 77, 60–68.
Mäder, U., Jenni, A., Lerouge, C., Gaboreau, S., Miyoshi, S., Kimura, Y., Cloet, V., Fukaya, M., Claret, F., Otake, T., Shibata, M., Lothenbach, B., 2017. 5-year chemico-physical evolution of concrete-claystone interfaces. Swiss J. Geosci. (Accepted for publication).
Martin, F., Micoud, P., Delmotte, L., Marichal, C., Le Dred, R., De Parseval, P., Mari, A., Fortune, J.P., Salvi, S., Beziat, D., Grauby, O., Ferret, J., 1999. The structural formula of talc from the Trimouns Deposit, Pyrenees, France. Can. Mineral. 37, 997–1006.
Marty, N.C.M., Bildstein, O., Blanc, P., Claret, F., Cochepin, B., Su, D., Gaucher, E.C., Jacques, D., Lartigue, J.E., Mayer, K.U., Meeussen, J.C.L., Munier, I., Pointeau, I., Liu, S., Steefel, C.I., 2015. Benchmark for multicomponent reactive transport codes across a in the context of complex cement/clay interface. Comput. Geosci. 19, 635–653.
Massiot, D., Fayon, F., Capron, M., King, I., Le Calvé, S., Alonso, B., Durand, J.-O., Bujoli, B., Gan, Z., Hoatson, G., 2002. Modelling one- and two-dimensional solid-state NMR spectra. Magn. Reson. Chem. 40, 70–76.
Merlet, C., 1994. An accurate computer correction program for quantitative electron probe microanalysis. Microchim. Acta 114, 363–376.
Meunier, A., 2003. Argiles. GB Science Publisher, Paris.
Nagra, 2002. Project Opalinus Clay: Safety Report. Demonstration of Disposal Feasibility for Spent Fuel, Vitrified High-level Waste and Long-lived Intermediate Level Waste (Entsorgungsnachweis). Technical Report, NTB 02–05: Nagra, Wettingen, Switzerland.
Nied, D., Enemark-Rasmussen, K., L'Hopital, E., Skibsted, J., Lothenbach, B., 2016. Properties of magnesium silicate hydrates (M-S-H). Cem. Concr. Res. 79, 323–332.
ONDRAF/NIRAS, 2001. Towards a Sustainable Management of Radioactive Waste –Background to the SAFIR 2 Report, NIROND 2001–07 E, December 2001.
Pearson, F.J., Arcos, D., Bath, A., Boisson, J.-Y., Fernández, A.M., Gäbler, H.-E., Gaucher, E., Gautschi, A., Griffault, L., Hernán, P., Waber, H.N., 2003. Mont Terri Project – Geochemistry of Water in the Opalinus Clay Formation at the Mont Terri Rock Laboratory. Switzerland, Federal Office for Water and Geology (FOWG), Bern. Geology Series 5.
Pearson, F.J., Tournassat, C., Gaucher, E.C., 2011. Biogeochemical processes in a clay formation in situ Experiment: Part E: equilibrium controls on chemistry of pore water from the Opalinus Clay, Mont Terri underground research laboratory, Switzerland. Appl. Geochem. 26, 990–1008.
Poinssot, C., Fillet, C., Gras, J.M., 2010. Post-containment performance of geological repository systems: source-term release and radionuclide migration in the near- and far-field environments. In: Ahn, J., Apted, M.J. (Eds.), Geological Repository Systems for Safe Disposal of Spent Nuclear Fuels and Radioactive Waste. Woodhead Publishing, pp. 421–493.
Prêt, D., 2003. Nouvelles méthodes quantitatives de cartographie de la minéralogie et de la porosité dans les matériaux argileux: application aux bentonites compactées des barrières ouvragées. PhD thesis. University of Poitiers, France, p. 257.
Prêt, D., Sammartino, S., Beaufort, D., Fialin, M., Sardini, P., Cosenza, P., Meunier, A., 2010. A new method for quantitative petrography based on image processing of chemical element maps: Part II. Semi-quantitative porosity maps superimposed on mineral maps. Am. Mineral. 95, 1389–1398.
Ramırez, S., Vieillard, P., Bouchet, A., Cassagnabère, A., Meunier, A., Jacquot, E., 2005. Alteration of the Callovo–Oxfordian clay from Meuse-Haute Marne underground laboratory (France) by alkaline solution. I. A XRD and CEC study. Appl. Geochem. 20, 89–99.
Read, D., Glasser, F.P., Ayora, C., Guardiola, M.T., Sneyers, A., 2001. Mineralogical and microstructural changes accompanying the interaction of Boom Clay with ordinary Portland cement. Adv. Cem. Res. 13, 175–183.
Roosz, C., Grangeon, S., Blanc, P., Montouillout, V., Lothenbach, B., Henocq, P., Giffaut, E., Vieillard, P., Gaboreau, S., 2015. Crystal structure of magnesium silicate hydrates (M-S-H): the relation with 2:1 Mg–Si phyllosilicates. Cem. Concr. Res. 73, 228–237.
Sammartino, S., Siitari-Kauppi, M., Meunier, A., Sardini, P., Bouchet, A., Tevissen, E., 2002. An imaging method for the porosity of sedimentary rocks: adjustment of the PMMA method - example of a characterization of a calcareous shale. J. Sediment. Res. 72, 937–943.
Sánchez, L., Cuevas, J., Ramírez, S., Riuiz De León, D., Fernández, R., Vigil Dela Villa, R., Leguey, S., 2006. Reaction kinetics of FEBEX bentonite in hyperalkaline conditions resembling the cement–bentonite interface. Appl. Clay Sci. 33, 125–141.
Savage, D., Bateman, K., Hill, P., Hughes, C., Milodowski, A., Pearce, J., Rae, E., Rochelle, C., 1992. Rate and mechanism of the reaction of silicates with cement pore fluids. Appl. Clay Sci. 7, 33–45.
Savage, D., Benbow, S., 2007. Low pH cements. SKI Rep. 2007, 32.
Savage, D., 2014a. Constraints on cement-clay interaction. Water Rock Interact. [WRI 14] Procedia Earth Planet. Sci. 7, 770–773.
Savage, D., 2014b. Assessment of the Impact of the Long Term Evolution of Engineered Structures on the Safety-relevant Functions of the Bentonite Buffer in a HLW Repository. NAGRA Report NTB 13–02.
SKB, 2006. Long-term Safety for KBS-3 Repositories at Forsmark and Laxemar—a First Evaluation. Main and Shotcrete with Claystones in a Deep Disposal Context 355 Report of the SR-can Project. SKB Technical Report TR-06-09. Swedish Nuclear fuel and Waste Management Company, Stockholm. SKB Technical Report TR-06–09, 1–16.
Techer, I., Bartier, D., Boulvais, P., Tinseau, E., Suchorski, K., Cabrera, J., Dauzeres, A., 2012. Tracing interactions between natural argillites and hyper-alkaline fluids from engineered cement paste and concrete: chemical and isotopic monitoring of a 15-years old deep-disposal analogue. Appl. Geochem. 27, 1384–1402.
Tinseau, E., Bartier, D., Hassouta, L., Devol-Brown, I., Stammose, D., 2006. Mineralogical characterization of the Tournemire argillite after in situ interaction with concretes. Waste Manag. 26, 789–800.
Trotignon, L., Devallois, V., Peycelon, H., Tiffreau, C., Bourbon, X., 2007. Predicting the long term durability of concrete engineered barriers in a geological repository for radioactive waste. Phys. Chem. Earth, Parts A/B/C 32, 259–274.
Vinsot, A., Appelo, C.A.J., Cailteau, C., Wechner, S., Pironon, J., De Donato, P., De Cannière, P., Mettler, S., Wersin, P., Gabler, H.E., 2008. CO_2 data on gas and pore water sampled in situ in the Opalinus Clay at the Mont Terri rock laboratory. Phys. Chem. Earth Supplement 1 (33), S54–S60.
Wang, A., Freeman, J., Kuebler, K.E., 2002. Raman spectroscopic characterization of phyllosilicates. Lunar Planet. Sci. XXXIII, 1374.
Wiewiora, A., Weiss, Z., 1990. Crystallochemical classifications of phyllosilicates based on the unified system of projection of chemical composition: II. the chlorite group. Clay Miner. 25, 83–92.
Wojdyr, M., 2010. Fityk: a general-purpose peak fitting program. J. Appl. Crystallogr. 43, 1126–1128.